HHS Public Access

Author manuscript

Cell Rep. Author manuscript; available in PMC 2023 May 09.

Published in final edited form as:

Cell Rep. 2023 March 28; 42(3): 112182. doi:10.1016/j.celrep.2023.112182.

Inter-axonal molecular crosstalk via Lumican proteoglycan sculpts murine cervical corticospinal innervation by distinct subpopulations

Yasuhiro Itoh[1,5], **Vibhu Sahni**[1,2,3,5], **Sara J. Shnider**[1,4], **Holly McKee**[1], **Jeffrey D. Macklis**[1,6,*]

[1]Department of Stem Cell and Regenerative Biology and Center for Brain Science, Harvard University, Cambridge, MA 02138, USA

[2]Present address: Burke Neurological Institute, White Plains, NY 10605, USA

[3]Present address: Feil Family Brain and Mind Research Institute, Weill Cornell Medicine, New York, NY 10065, USA

[4]Present address: Teva Pharmaceuticals, Netanya 4250483, Israel

[5]These authors contributed equally

[6]Lead contact

SUMMARY

How CNS circuits sculpt their axonal arbors into spatially and functionally organized domains is not well understood. Segmental specificity of corticospinal connectivity is an exemplar for such regional specificity of many axon projections. Corticospinal neurons (CSN) innervate spinal and brainstem targets with segmental precision, controlling voluntary movement. Multiple molecularly distinct CSN subpopulations innervate the cervical cord for evolutionarily enhanced precision of forelimb movement. Evolutionarily newer $CSN_{BC\text{-}lat}$ exclusively innervate bulbar-cervical targets, while CSN_{medial} are heterogeneous; distinct subpopulations extend axons to either bulbar-cervical or thoraco-lumbar segments. We identify that Lumican controls balance of cervical innervation between $CSN_{BC\text{-}lat}$ and CSN_{medial} axons during development, which is maintained into maturity. Lumican, an extracellular proteoglycan expressed by $CSN_{BC\text{-}lat}$, non-cell-autonomously suppresses cervical collateralization by multiple CSN_{medial} subpopulations. This inter-axonal molecular crosstalk between CSN subpopulations controls murine corticospinal circuitry refinement and forelimb dexterity. Such crosstalk is generalizable beyond the corticospinal system for evolutionary incorporation of new neuron populations into preexisting circuitry.

*Correspondence: jeffrey_macklis@harvard.edu.

AUTHOR CONTRIBUTIONS

Research designed by Y.I., V.S., S.J.S., and J.D.M.; research performed by Y.I., V.S., S.J.S., and H.M.; data analyzed by Y.I., V.S., S.J.S., and J.D.M.; and manuscript written by Y.I., V.S., and J.D.M.

DECLARATION OF INTERESTS

The authors declare no competing interests.

SUPPLEMENTAL INFORMATION

Supplemental information can be found online at https://doi.org/10.1016/j.celrep.2023.112182.

In brief

Itoh et al. demonstrate that the extracellular proteoglycan Lumican controls balance of cervical innervation between distinct corticospinal neuron (CSN) subpopulations (bulbar-cervical projecting $CSN_{BC\text{-}lat}$ vs. diverse CSN_{medial}) via non-cell-autonomous inter-axonal crosstalk. This mechanism controls corticospinal circuitry refinement and forelimb dexterity in mice and potentially enabled evolutionary diversification of corticospinal circuitry.

Graphical Abstract

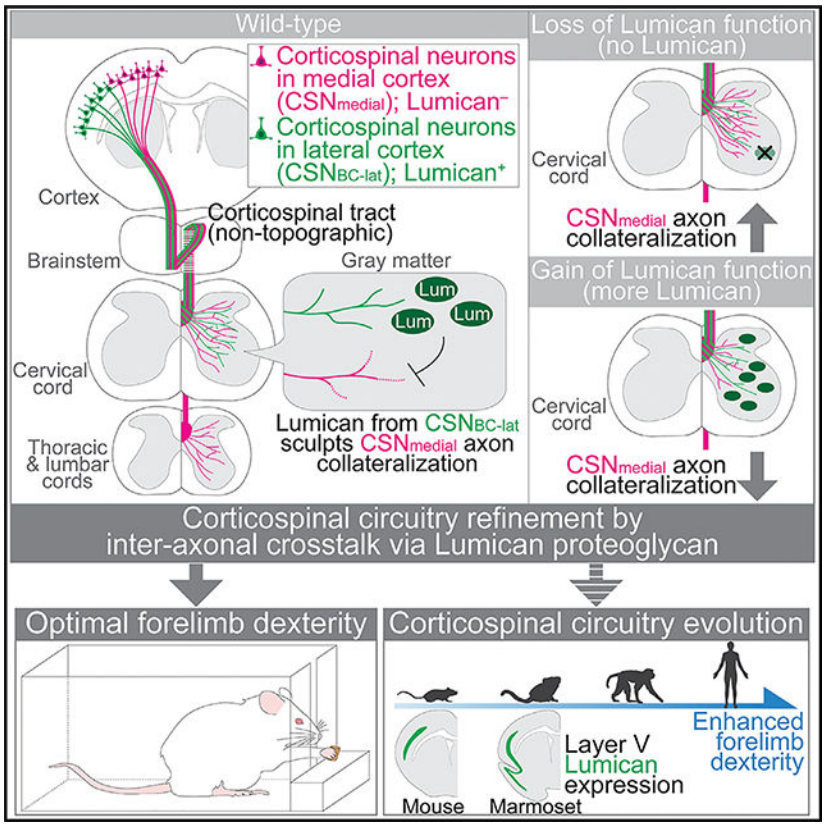

INTRODUCTION

A central question in complex CNS circuitry is how multiple convergent afferent sources are balanced and sculpted at the level of axonal arbors into spatial and functional domains.[1,2] Ultimate integration of interdigitated inputs in the same area is critically important to CNS function; for some spatially discrete inputs, there are known solutions for their organization and integration, e.g., topographic retinotectal projections. However, mechanisms underlying appropriate afferent balance in spatially integrated domains remain to be elucidated. Although activity-dependent events contribute to regulation of relative afferent balance, it is likely that early circuit development establishes the foundation for proper axonal arbor proportions and relative afferent balance in interdigitated territories.[1,3] Of particular interest, there has been evolutionary expansion of diversity and subtlety of CNS circuitry, likely requiring at least some exclusion of evolutionarily older circuitry. Segmental specificity of

corticospinal connectivity—with its evolutionary addition of progressively refined cervical innervation for new and enhanced forelimb functions—is an exemplar for such regional intercalation of multiple afferents and for evolutionary insertion of new circuits in domains of evolutionarily older circuitry.

Corticospinal neurons (and related cortico-brainstem neurons; together "CSN") extend axons to subcerebral targets and make synaptic connections with circuits in the brainstem and spinal cord.[1,4,5] CSN axons form the corticospinal tract (CST), the major output pathway from the cortex and the principal circuit for skilled movements.[6,7] Most CSN ultimately control voluntary movements by coordinating specific functional motor groups, limb sections, or individual digits.[5] The repertoire of skilled movement, such as speech and precise forelimb/digit movement, has expanded significantly through mammalian evolution: this dramatic expansion is associated with a concomitant evolutionary increase in numbers of CSN axons innervating these subcerebral targets and evolutionary expansion of cortical territories originating these projections.[6,8,9] Ultimate execution of such fine motor control necessitates that cortical efferents establish diverse yet precise innervation of segmentally specific spinal and brainstem circuits[6,8,9]; how this is established during development remains essentially unknown.

Importantly, CSN exhibit striking anatomical and functional diversity[9–18]; some CSN extend axons to brainstem and cervical targets to control face and arm movement, while others extend axons to thoraco-lumbar targets to control trunk and leg movement. Further, CSN have subsets in multiple cortical areas, spanning far beyond the primary motor cortex (M1). CSN in rostrolateral sensorimotor cortex are evolutionarily newer and exclusively innervate bulbar-cervical targets (referred to here as $CSN_{BC\text{-}lat}$; Figure 1A). In contrast, CSN in caudomedial sensorimotor cortex, including M1, are evolutionarily older and are relatively more heterogeneous (referred to here as CSN_{medial}; Figure 1A), with interdigitated subpopulations extending axons to either bulbar-cervical or thoraco-lumbar spinal cord, maintained from early development into maturity.[19–22] Thus, CSN_{medial} can be further subdivided into $CSN_{BC\text{-}med}$ and CSN_{TL}, respectively.[22,23] Molecular controls have been elucidated that govern specification and differentiation of distinct neocortical projection neuron subtypes, including CSN/subcerebral projection neurons (SCPN; CSN are a subset of SCPN). CSN differentiation is controlled across temporal, subtype, and areal axes,[24,25] with interplay between CSN and other cell types.[26,27] We investigated CSN diversity and identified that anatomically distinct CSN subpopulations are also molecularly distinct, revealing intrinsic molecular controls over CSN axon extension to distinct spinal levels.[22,23] However, it remained unclear how subsequent axon collateral development by these distinct CSN subpopulations is molecularly regulated.[2,28]

Of note, the cervical cord, which coordinates skilled forelimb/arm movements, receives inputs from multiple cortical areas spanning beyond M1[8,17,18] and is innervated by all three CSN subpopulations ($CSN_{BC\text{-}lat}$, $CSN_{BC\text{-}med}$, and CSN_{TL}).[22] This raises a fundamental question regarding how distinct CSN subpopulations elaborate the appropriate contribution of axon collaterals into the cervical gray matter—how axon collateralization is sculpted or spatially shaped[29] and whether there is competitive crosstalk between axons of these distinct CSN subpopulations.

Lumican belongs to the family of extracellular matrix (ECM) proteins called small leucine-rich proteoglycans (SLRPs). *Lumican* encodes a 12 leucine-rich repeat (LRR)-containing ECM protein that is conserved across vertebrates,[30–32] and many similar ECM proteins have been shown to regulate axon guidance and targeting.[33,34] Although Lumican has been studied in a variety of tissues—notably the cornea and connective tissues—in the context of development, immunity, or cancer,[30,31] its expression or function during mammalian neural development remains relatively unstudied and thus poorly understood.[35]

Here, we identify that Lumican is expressed specifically by $CSN_{BC\text{-}lat}$ in developing mouse cortex; controls axon collateralization by CSN_{medial} (both $CSN_{BC\text{-}med}$ and CSN_{TL}) in the cervical cord in a non-cell-autonomous, crosstalk manner; and contributes significantly to optimal forelimb dexterity. This mechanism highlights a form of inter-subpopulation control over establishing balanced innervation, whereby a secreted molecule from one CSN subpopulation mediates inter-axonal expulsion, potentially generalizable to other circuitry. Our results and their implications might elucidate how evolutionarily newer CSN integrate into evolutionarily preexisting circuitry and how this enables diversification of circuitry for more-refined motor function.

RESULTS

Lumican is specifically and transiently expressed by $CSN_{BC\text{-}lat}$ in postnatal mouse cortex

Lumican emerged from our prior work as a particularly interesting candidate for controlling CSN axon collateralization. *Lumican* is specifically expressed postnatally by CSN vs. callosal projection neurons (CPN).[36] In recent work,[22,23] transcriptional profiling identified genes differentially expressed between developing $CSN_{BC\text{-}lat}$ and CSN_{medial} (Figure 1A). We identified *Lumican* as strikingly differentially expressed by $CSN_{BC\text{-}lat}$ compared with almost no detectable expression by CSN_{medial} (Figure 1B). This differential expression increases from postnatal day (P) 1 to P7 (Figure 1B), when CSN axons are growing in the spinal cord, suggesting that Lumican might function in development and/or specificity of circuitry between cortex and bulbar-cervical targets.

We investigated the time course and cell-type-specific expression of Lumican in postnatal neocortex. *In situ* hybridization at P4, P7, and P13 revealed that *Lumican* expression is strikingly restricted to layer V in lateral sensorimotor cortex, where $CSN_{BC\text{-}lat}$ reside, and is excluded from medial cortex, where CSN_{medial} reside (Figures 1C–1E), consistent with differential gene expression analyses described above (Figure 1B). *Lumican* expression in lateral cortex increases from P4 to P7 and is maintained at P13 (Figures 1C–1E). Immunocytochemical analyses additionally confirm that Lumican expression is confined to layer V in lateral cortex at P4 and P8 (Figures 1F, 1G, S1A, and S1B). Importantly, Lumican protein is more abundant rostrolaterally and absent medially in M1 and secondary motor cortex (M2) (Figures 1F and S1A–S1C). Neocortical Lumican expression remains restricted to lateral layer V at P14, although at a lower level, and becomes undetectable by P21 (Figure S1D).

We next investigated whether Lumican is expressed only by SCPN in lateral cortex. The overwhelming majority of Lumican-positive cells (88.1% ± 2.0%) also express high-

level CTIP2, an SCPN-specific control at high expression levels.[36] A fraction of Lumican-expressing cells (24.2% ± 5.1%) also express SATB2, a CPN developmental control,[37,38] which is also expressed by ~20%–40% of CTIP2-expressing SCPN earlier in development[39] (Figures 1F–1H and S1A). Importantly, the vast majority (95%) of $SATB2^+$/$Lumican^+$ double-positive neurons also express CTIP2. Together, these results strongly indicate that Lumican is expressed specifically by SCPN in rostrolateral sensorimotor cortex. We further directly investigated whether Lumican is expressed by SCPN by performing retrograde analysis. Virtually all (>99%) Lumican-expressing cells in lateral cortex are retrogradely labeled from the cerebral peduncle (Figure S1E), demonstrating that Lumican is expressed specifically by a subset of SCPN in lateral cortex. Finally, we investigated Lumican expression in *Fezf2* null cortex, which completely and specifically lacks CSN and other SCPN.[40,41] Strikingly, Lumican expression is completely absent in *Fezf2* null cortex (Figure 1I), confirming by independent approaches that Lumican is expressed essentially only by lateral SCPN.

We further and more broadly investigated Lumican expression throughout the CNS. In the postnatal forebrain, Lumican expression is highly restricted; in addition to SCPN in lateral cortex, Lumican is expressed by only a subset of caudoventral hippocampal cells (Figure S1C). Lumican is also expressed by meningeal cells, encapsulating the CNS (Figures S1B–S1H). Apart from this meningeal expression, there is no detectable *Lumican* expression in the spinal parenchyma: Lumican is not detectably expressed by neurons or glia in the spinal cord (Figures S1G and S1H). We do detect weak Lumican signal within the spinal cord, but this signal co-localizes with an endothelial marker, PECAM-1, which indicates Lumican expression by blood vessels at lower levels (Figures S1G and S1H). We confirmed the specificity of the antibody used in these analyses by verifying that observed expression is abolished in *Lumican* null mice (Figure S1B). Taken together, Lumican is highly specifically and transiently expressed by SCPN in lateral cortex during postnatal development and is absent from adult SCPN.

We next directly investigated whether Lumican is expressed by $CSN_{BC\text{-}lat}$ by combining Lumican immunocytochemistry with retrograde analysis. We retrogradely labeled all CSN from the cervical dorsal funiculus at P4, labeling all CSN in both medial and lateral cortex. Lumican is expressed by CSN in lateral cortex (Figure 1J). Notably, there is a striking and almost complete exclusion of Lumican from CSN in medial cortex (Figure 1J). The fraction of Lumican-expressing CSN is significantly higher in lateral vs. medial rostral sensorimotor cortex (40.0% ± 19.2% vs. 7.7% ± 4.1%, respectively; mean ± SD; $p < 0.05$, unpaired two-tailed t test; Figure 1J). Together, these results identify that Lumican is expressed by $CSN_{BC\text{-}lat}$ and not expressed by CSN_{medial} (Figure 1K).

Proteoglycans, including Lumican and, in particular, keratan sulfate proteoglycans (KSPGs), are primarily ECM proteins, many of which have known functions in regulating axon path-finding during development and limiting plasticity following CNS injury.[32–34,42–45] Lumican core protein undergoes posttranslational modification via N-linked glycans, which in certain instances are further modified via addition of keratan sulfate glycosaminoglycan (GAG) chains to exist as a KSPG.[30–32,46]

We therefore investigated whether Lumican expressed in the CNS undergoes either of these modifications. We dissected lateral sensorimotor cortex and cervical cord from wild-type and *Lumican* null mice, followed by careful removal of meningeal membranes (Figure S1I), then examined Lumican expression in these tissues by western blotting (Figure S1J). In wild-type cortex and spinal cord, we detect a 42 kDa band (likely core protein) and a 55–75 kDa band (likely proteoglycan)[46]; both bands are absent in *Lumican* null mice (Figure S1J). Since these molecular weights are lower than that of corneal Lumican (Figure S1J), which contains highly sulfated GAG chains,[47] this suggests that Lumican GAG chains in the CNS are shorter or less sulfated compared with those on corneal Lumican.

We next compared Lumican protein abundance between cervical and lumbar segments via western blotting. Lumican abundance in the cervical cord is significantly higher than that in the lumbar cord (Figure S1K). Importantly, we find that Lumican protein is efficiently secreted into the culture medium when overexpressed by cultured cortical primary neurons *in vitro* (Figure S1L). These results indicate that $CSN_{BC\text{-}lat}$-derived cervical Lumican undergoes posttranslational modifications and that Lumican is efficiently secreted by neurons, consistent with previous findings that Lumican is secreted by other cell types, such as fibroblasts.[30]

Lumican suppresses CSN_{medial} axon collateralization in the cervical spinal cord, in a non-cell-autonomous manner

Lumican is expressed by $CSN_{BC\text{-}lat}$ in the first 2 postnatal weeks, with peak expression between P7 and P14 (Figure 1 and S1). This occurs just after initial CSN axon segment-level targeting decisions have largely been made; CSN axons have already reached their target spinal segments in the CST[22,23,48,49] and are extending collaterals into the spinal gray matter.[50] Thus, this timing of peak expression suggested that Lumican might likely control CSN axon collateralization rather than initial axon targeting.

Even more intriguingly, Lumican is expressed selectively by $CSN_{BC\text{-}lat}$ that extend axons only to bulbar-cervical segments. Cervical segments are also innervated by many CSN_{medial},[22] which do not express Lumican (Figure 1J). Further, cortical neurons secrete Lumican (Figure S1L), suggesting that $CSN_{BC\text{-}lat}$-derived Lumican might function in a non-cell-autonomous manner and regulate CSN_{medial} axon collateralization in the cervical cord. Given the known inhibitory effects of KSPGs on axon growth and sprouting,[43–45] we hypothesized that Lumican might limit CSN_{medial} axon collateralization in the cervical cord.

To test this hypothesis, we investigated CSN_{medial} axon collateralization in wild-type and *Lumican* null mice, using biotinylated dextran amine (BDA) labeling (Figure 2A). We selected mice with identical injections (Figures 2A–2C and S2A) for further unbiased and automated analysis of BDA-labeled CSN_{medial} axon collateralization in the cervical cord, with blinded criteria established *a priori* (Figures 2D–2I, S2B, and S2C).

Our experiments reveal that deletion of *Lumican* specifically de-represses CSN_{medial} collateralization in the cervical cord. BDA-labeled CSN_{medial} axons traversed the CST normally and unilaterally in the cervical dorsal funiculus in *Lumican* null mice, without any defects in midline crossing, and a similar subset of CSN_{medial} axons reached the

lumbar segment in both wild-type and *Lumican* null mice (Figures 2D, 2E, and S2B). Axial sections at cervical C1–C2 showed visibly more exuberant axon collaterals in cervical gray matter in *Lumican* null vs. wild-type mice (Figures 2D and 2E). Since CSN_{medial} axons extend collaterals throughout the rostrocaudal extent of cervical gray matter,[22] we investigated CSN_{medial} axon collateralization across the entire cervical gray matter (from C3 to C8). Again, there is a dramatic increase in CSN_{medial} axon collateralization across C3–C8 in *Lumican* null mice (Figures 2F and 2G). We traced the total collateral area across C3–C8 gray matter (see STAR Methods) and normalized this area to the total number of labeled CSN_{medial} axons in the dorsal funiculus at C1–C2 to determine the approximate collateral target density for each BDA-labeled CSN_{medial} axon (Figures 2D–2I and S2C). This quantification shows increased CSN_{medial} axon collateral density in *Lumican* null mice compared with wild-type mice (Figure 2I). Since CSN_{medial} do not express Lumican (Figure 1), this result indicates that CSN_{medial} axon collateralization in the cervical cord is suppressed by Lumican in a non-cell-autonomous manner.

We next investigated axon collateralization in cervical gray matter by $CSN_{BC\text{-}lat}$, which normally themselves express Lumican (Figure 2J). Wild-type $CSN_{BC\text{-}lat}$ axon collaterals are most abundant in the intermediate gray matter dorsoventrally at cervical C1–C2[22] (Figure 2J). In striking contrast to CSN_{medial}, the density of cervical axon collaterals of $CSN_{BC\text{-}lat}$ in *Lumican* null mice does not show a significant change compared with wild-type mice; rather, though not significantly, $CSN_{BC\text{-}lat}$ axons even display a trend toward modest reduction in their cervical spinal collateral density (Figure 2J; also see discussion).

Together, these findings demonstrate that Lumican, produced by $CSN_{BC\text{-}lat}$, non-cell-autonomously limits and relatively excludes CSN_{medial} axon collateralization in cervical cord.

CSN specification and main axon extension is unchanged in *Lumican* null mice

Given the highly specific Lumican expression by $CSN_{BC\text{-}lat}$ in the postnatal CNS, we hypothesized that increased CSN_{medial} axon collateralization in *Lumican* null mice is specifically mediated by loss of Lumican expression by $CSN_{BC\text{-}lat}$ rather than by some theoretically broader, non-specific defect in cortical organization. To rigorously test this hypothesis, we investigated earlier stages of cortical projection neuron specification in *Lumican* null mice. We found that wild-type and *Lumican* null mice are indistinguishable in their overall brain size or in their expression and laminar organization of CTIP2, SATB2, and Tbr1, a corticothalamic projection neuron (CThPN) marker and control (Figure 3A), confirming that Lumican does not function in early cortical development or cortical projection neuron specification. We further found that $CSN_{BC\text{-}lat}$ genes (*Klhl14* and *Cartpt*) and CSN_{medial} genes (*Crymu* and *Crim1*)[22] are specifically expressed laterally and medially, respectively, in layer V at P4 in both wild-type and *Lumican* null mice (Figure 3B). Together, these data indicate that CSN are generated and specified normally in the absence of *Lumican*.

We next investigated the theoretical possibility that abnormal CSN_{medial} axon collateralization in *Lumican* null mice arises as a secondary consequence of abnormalities of initial CST axon segmental targeting. Injection of cholera toxin B subunit (CTB) at the

most rostral level of cervical segment (C1) retrogradely labels all CSN. Both wild-type and *Lumican* null mice have efficient retrograde labeling, exhibiting indistinguishable total numbers and distributions of retrogradely labeled CSN (Figure 3C), indicating that CSN axon extension to the spinal cord occurs normally in *Lumican* null mice. We also investigated CST axon extension using a genetic reporter; we crossed *Lumican* null mice with $Emx1^{IRES\text{-}Cre/IRES\text{-}Flpo}$;$Ai65^{RCFL\text{-}tdT/+}$ mice, which express tdTomato in all cortical projection neurons.[22] After decussation, all wild-type CST axons extend to cervical C1–C2, and then only a progressively diminishing subset of these axons extend to thoracic T1–T2 and lumbar L1–L2, consistent with prior work.[22,23,48] Axon guidance at the decussation and this rostrocaudal distribution of CST main axon projection remains unaffected in *Lumican* null mice (Figure 3D), indicating that Lumican does not control CST main axon extension.

Collectively, these results indicate that CSN specification and main axon extension occur normally in the absence of *Lumican*, indicating that the specificity of Lumican's effect on CSN_{medial} axon collateralization does not arise as a secondary consequence of abnormalities in CSN specification or CST main axon segmental targeting.

Lumican overexpression by $CSN_{BC\text{-}lat}$ suppresses CSN_{medial} axon collateralization in the cervical cord

To investigate whether $CSN_{BC\text{-}lat}$-derived Lumican directly suppresses CSN_{medial} axon collateralization, we next examined the effect of Lumican overexpression by $CSN_{BC\text{-}lat}$ on CSN_{medial} axon collateralization. At P1 or P2, we injected adeno-associated virus (AAV) encoding either EGFP alone (AAV-EGFP) or EGFP and Lumican (AAV-EGFP-2A-Lumican) rostrolaterally to specifically target $CSN_{BC\text{-}lat}$ in wild-type mice. We then used iontophoresis to stereotactically deliver BDA into caudomedial sensorimotor cortex in 4-week-old mice to analyze CSN_{medial} axon collateralization in the cervical cord (Figure 4A). We first confirmed that AAV and BDA labeling was specific to $CSN_{BC\text{-}lat}$ and to CSN_{medial}, respectively (Figures 4B–4E and S3A). We observed the expected level of previously described BDA-labeled CSN_{medial} axon collaterals across the rostrocaudal extent of the cervical spinal cord in control AAV-EGFP rostrolaterally injected mice (Figures 4D and 4F). In striking contrast, Lumican overexpression by $CSN_{BC\text{-}lat}$ dramatically reduced CSN_{medial} axon collateralization in the cervical cord, throughout the rostrocaudal and dorsoventral extent of the cervical cord (Figures 4E and 4G). Quantification of relative collateral density of labeled CSN_{medial} axons shows substantial reduction in AAV-EGFP-2A-Lumican- vs. AAV-EGFP-injected mice (Figure 4H). We further investigated whether Lumican derived exclusively from $CSN_{BC\text{-}lat}$ axons is sufficient to suppress CSN_{medial} axon collaterals in the cervical cord by overexpressing Lumican in *Lumican* null mice. When compared with the result of Lumican overexpression in wild-type mice, CSN_{medial} axon collateral density in *Lumican* null mice is efficiently reduced to a similar level, strongly suggesting that Lumican overexpression by $CSN_{BC\text{-}lat}$ efficiently and reproducibly suppresses exuberant CSN_{medial} axon collaterals in *Lumican* null mice (Figure S3B). Together, these results strongly reinforce that $CSN_{BC\text{-}lat}$-derived Lumican suppresses CSN_{medial} axon collateralization in a non-cell-autonomous manner.

It is theoretically possible that Lumican promotes $CSN_{BC\text{-}lat}$ axon collateralization cell autonomously, then secondarily suppresses CSN_{medial} axon collateralization. To investigate which CSN axons primarily respond to Lumican, we overexpressed Lumican by CSN_{medial} or $CSN_{BC\text{-}lat}$ via AAV and investigated cell-autonomous effects on axon collateral density. We injected AAV-EGFP or AAV-EGFP-2A-Lumican into wild-type mouse cortex caudomedially to target CSN_{medial} or rostrolaterally to target $CSN_{BC\text{-}lat}$, then analyzed $EGFP^+$ axon collaterals in the spinal cord. The data reveal that Lumican overexpression by CSN_{medial} substantially reduces CSN_{medial} axon collateral density in cervical and thoracic segments (Figure S3C), but Lumican overexpression by $CSN_{BC\text{-}lat}$ does not change $CSN_{BC\text{-}lat}$ axon collateral density in the cervical segment (Figure S3D). These results indicate that CSN_{medial} axons primarily respond to Lumican.

Given the CSN axon collateralization phenotype in cervical cord in *Lumican* null mice, without any discernible effect on CSN main axon extension (Figures 3C and 3D), we hypothesized that Lumican expressed by $CSN_{BC\text{-}lat}$ suppresses CSN_{medial} axon collateralization locally in the spinal cord. We first investigated whether Lumican is trafficked to CSN axons. We overexpressed Lumican rostrolaterally in cortex in wild-type mice and find that, consistent with this hypothesis, Lumican protein is present within $CSN_{BC\text{-}lat}$ axons in the cervical cord (Figure S3E). We also identified that endogenous Lumican protein is present in the cervical cord (Figures S1J and S1K), and that Lumican is efficiently secreted by primary neurons (Figure S1L), together suggesting that Lumican is anterogradely trafficked in $CSN_{BC\text{-}lat}$ axons and likely secreted by these axons in the cervical cord.

We further investigated whether Lumican misexpression locally in the cervical cord suppresses CSN_{medial} axon collateralization (Figure S3F). AAV-EGFP or AAV-EGFP-2A-Lumican was injected into cervical gray matter at P1, and CSN_{medial} were labeled by AAV encoding tdTomato delivered into caudomedial sensorimotor cortex at P4. We find that Lumican misexpression in cervical cord substantially decreases CSN_{medial} axon collateral density at P25 (Figure S3F), indicating that Lumican can function locally in cervical cord to suppress CSN_{medial} axon collateralization. Together, these results strongly support the interpretation that $CSN_{BC\text{-}lat}$-derived Lumican suppresses CSN_{medial} axon collaterals locally in the cervical cord.

We speculated that Lumican might suppress axon collateralization by binding to transmembrane proteins on axonal membranes; Lumican is reported to bind secreted and cell-surface molecules, modulating intracellular signaling.[30] We used a cell-surface binding assay[51,52] to investigate potential Lumican binding to select candidate transmembrane proteins (Figure S4A), based on their: (1) higher expression by CSN_{medial},[22] (2) previously known interaction with Lumican,[30] and/or (3) potential LRR-binding motif.[53,54] None of these candidates reveal significant binding to Lumican (Figures S4A–S4C). We also investigated whether exogenously added Lumican binds neural tissue, using an on-section binding assay[55] that probes potential bait interactions with both transmembrane and secreted structural matrix proteins. Other than meningeal or blood vessel binding, no Lumican binding was detected in the cortex or cervical cord (Figures S4D–S4G). Lumican likely binds to collagen type I in meninges and blood vessels,[31,56] unlikely to underlie the effects

on CSN axon collateralization. These results suggest that Lumican might regulate CSN axon collateralization by binding to secreted non-structural molecules.

We further explored potential Lumican-containing molecular complexes in an unbiased manner, by conducting liquid chromatography with ultra-low-input tandem mass spectrometry (LC-MS/MS) on Lumican complex isolated from developing cervical cord by immunoprecipitation (IP). We immunoprecipitated Lumican protein complex from P7–P10 cervical spinal cord of *Lumican* null mice (negative control), wild-type mice, and *Lumican* null mice that received AAV-EGFP-2A-Lumican injection into sensorimotor cortex at P1 (Lumican overexpression mice). This IP-MS analysis identified >100 proteins at high stringency (Figure S4H). Importantly, Lumican protein is substantially enriched (2^4- to 2^5-fold) in both wild-type mice and Lumican overexpression mice. The majority of the protein species identified by this analysis are intracellular proteins, and many of them are trafficking-related proteins, consistent with our results that Lumican is secreted. However, very few transmembrane or extracellular proteins were identified by the MS approach employed to isolate multiprotein complexes optimally, and none of the classic axon guidance molecules, such as Slits or Semaphorins, were identified (Figure S4H). Only two extracellular proteins suggested minor enrichment in both wild-type mice and Lumican overexpression mice compared with *Lumican* null mice: Aquaporin 4 and Mfge8 (milk-fat globule EGF and factor V/VIII-containing). We further investigated Mfge8, given its known phagocytic functions in the immune system.[57] To further investigate whether Mfge8 binds to Lumican, we immunoprecipitated the Mfge8 protein complex from developing mouse cervical cord, followed by LC-MS/MS analysis. While about 300 protein species are identified with high stringency in association with Mfge8, with substantial enrichment of Mfge8 protein by IP with anti-Mfge8 antibody over a corresponding control antibody (2^7-fold), Lumican protein was not identified in the complex (Table S1).

Lumican suppresses both bulbar-cervical and thoracolumbar CSN_{medial} subpopulations: Intersectional AAV labeling identifies that $CSN_{BC\text{-}med}$ axon collateralization is increased in *Lumican* null cervical cord

We have thus far used spatial locations of CSN within sensorimotor cortex (rostrolateral vs. caudomedial) to investigate CSN axon collateralization. However, CSN_{medial} are recently known to comprise at least two distinct subpopulations: the more commonly considered CSN_{TL} that extend thoracolumbar projections and the developmentally and molecularly distinct $CSN_{BC\text{-}med}$ that extend axons exclusively to bulbar-cervical segments (Figure 5A).[22] BDA or AAV injections into caudomedial sensorimotor cortex, as described earlier, label both $CSN_{BC\text{-}med}$ and CSN_{TL}. Importantly, axons of both subpopulations extend collaterals into cervical gray matter, although by CSN_{TL} at much lower density.[22] We therefore next investigated whether Lumican regulates axon collateralization by only one or by both CSN_{medial} subpopulations. Since $CSN_{BC\text{-}med}$ and CSN_{TL} reside in a spatially interdigitated manner in caudomedial sensorimotor cortex,[22] this necessitated more advanced approaches than conventional anterograde tracing to investigate axon collateralization by these two distinct subpopulations. We applied two independent approaches—intersectional viral labeling (Figures 5B–5E and S5), which uses their segmentally distinct axon projections,

and intersectional mouse genetics (Figures 6 and S6), which takes advantage of the fact that $CSN_{BC\text{-}med}$ and CSN_{TL} are molecularly distinct—to distinguish the two subpopulations.

We first investigated whether $CSN_{BC\text{-}med}$ axon collateralization is regulated by Lumican. We utilized an intersectional viral labeling approach for exclusionary, subtractive labeling of the two CSN subpopulations within caudomedial sensorimotor cortex (see STAR methods). As schematized in Figure 5B, CSN_{TL} are labeled by EGFP (turboRFP$^+$;EGFP$^+$ or turboRFP$^-$;EGFP$^+$), while $CSN_{BC\text{-}med}$ remain singly positive for turboRFP (turboRFP$^+$;EGFP$^-$) (Figure S5A). We investigated axon extension by EGFP-positive and turboRFP-single-positive CSN axons in the dorsal funiculus at cervical and thoracic levels (Figures S5B and S5C). The percentages of turboRFP-single positive axons at C1–C2 that extend to T1–T2 are indistinguishable between wild-type and *Lumican* null mice. This approach enabled investigation of $CSN_{BC\text{-}med}$ axon collateralization as a distinctly labeled subset within the overall CSN_{medial} subpopulation.

We next quantitatively compared the target density of $CSN_{BC\text{-}med}$ axon collaterals in cervical gray matter between wild-type and *Lumican* null mice. Given the theoretical possibility that Lumican might control $CSN_{BC\text{-}med}$ axon collateralization variably at distinct levels of the cervical cord, we analyzed axon collateralization in axial sections of the cervical cord at three distinct segments: C1–C2, C3–C4, and C5–C6. We find that $CSN_{BC\text{-}med}$ axon collateral density is increased from C3 to C6 in *Lumican* null compared with wild-type mice (Figures 5C–5E). Interestingly, $CSN_{BC\text{-}med}$ axon collateral density remains unchanged at C1–C2 in *Lumican* null mice. These results indicate that $CSN_{BC\text{-}med}$ axon collateralization in cervical cord is suppressed by Lumican.

Lumican also suppresses thoraco-lumbar CSN_{medial} subpopulation: Intersectional genetic reporter labeling identifies that CSN_{TL} axon collateralization is increased in *Lumican* null cervical cord

Labeling a specific subset of neurons by mouse genetic tools provides a powerful, non-invasive approach for anatomical and functional investigation. The intersectional viral labeling approach described above enables enrichment of $CSN_{BC\text{-}med}$, but CSN_{TL} axons labeled using this approach are axotomized by the AAV-retro-Cre injection in the thoracic dorsal funiculus at P4. This could potentially modify more rostral collateral formation, thus interfering with accurate investigation of CSN_{TL} axon collateralization in the cervical cord. To circumvent this potential effect, we investigated CSN_{TL} axon collateralization using $Crim1^{GCE}$;$Emx1^{IRES\text{-}FlpO}$;Ai65$^{RCFL\text{-}tdT}$ intersectional genetic reporter mice.[22]

To investigate CSN_{TL} axon collateralization in the absence or presence of Lumican function, we crossed these triple-transgenic mice with *Lumican* null mice to generate *Lumican* wild-type; $Crim1^{GCE/+}$;$Emx1^{IRES\text{-}Flpo/IRES\text{-}Flpo}$;$Ai65^{RCFL\text{-}tdT/RCFL\text{-}tdT}$ or *Lumican* null;$Crim1^{GCE/+}$;$Emx1^{IRES\text{-}Flpo/IRES\text{-}Flpo}$;$Ai65^{RCFL\text{-}tdT/RCFL\text{-}tdT}$ mice. Both sets of mice were injected intraperitoneally with tamoxifen at P3 to label CSN_{TL} (Figures 6A and S6). We analyzed axon collateralization at 5 weeks of age in axial sections of the cervical cord at distinct segments. As previously described,[22] CSN_{TL} axons in both wild-type and *Lumican* null mice extend collaterals in the cervical gray matter at all these spinal segments. We find that CSN_{TL} have more exuberant collaterals in *Lumican* null compared with wild-type

mice (Figures 6B and 6C). Quantification of axon collateral density reveals increased axon collateralization by *Lumican* null CSN_{TL} throughout the cervical cord (Figure 6D). This demonstrates that Lumican also suppresses CSN_{TL} axon collateralization throughout the cervical cord.

We next investigated whether Lumican regulates the dorsoventral and mediolateral distribution of CSN_{TL} axon collateralization at cervical C3–C4 (Figures 6E and 6F). In wild-type mice, CSN_{TL} axon collaterals are present predominantly in the intermediate gray matter dorsoventrally: ~12% of CSN_{TL} axon collaterals are present in the dorsal-most quarter; very few CSN_{TL} collaterals (~7%) are present in the ventral-most quarter; ~81% of CSN_{TL} axon collaterals are present in the central half of the spinal gray matter (Figure 6F). Further, ~70% of CSN_{TL} axon collaterals are present in the medial half of the spinal gray matter, with very few (~7%) collaterals present in the lateralmost quarter (Figure 6E). This overall topography of CSN_{TL} axon collateral distribution is unaltered in *Lumican* null mice (Figures 6E and 6F). While proportionally increased throughout the mediolateral extent of the cord (Figure 6E), CSN_{TL} axon collateral density in *Lumican* null mice is relatively unchanged in either the dorsal or the ventral quarter (Figure 6F). In contrast, CSN_{TL} collateral density is significantly increased throughout the intermediate gray matter in *Lumican* null mice (Figure 6F), where axon collaterals of Lumican-expressing $CSN_{BC\text{-}lat}$ are also located (Figure 2J). These findings indicate that Lumican limits CSN_{TL} axon collateralization within its normal domain of cervical gray matter.

Given specific Lumican expression by $CSN_{BC\text{-}lat}$ that extend axons exclusively to bulbar-cervical segments, we investigated whether Lumican suppresses CSN axon collateralization in a segment-specific manner, by analyzing CSN_{TL} axons at thoracic T1–T2 and lumbar L1–L2. We first investigated CSN_{TL} main axon extension in the dorsal funiculus white matter. Consistent with the results using $Emx1^{IRES\text{-}Cre/IRES\text{-}Flpo};Ai65^{RCFL\text{-}tdT/+}$ mice (Figure 3D), there is no difference in CSN_{TL} main axon extension in the dorsal funiculus from C1–C2 to T1–T2 and to L1–L2 between wild-type and *Lumican* null mice (Figures 6G and 6H). We next investigated CSN_{TL} axon collateralization. In wild-type mice, when compared with CSN_{TL} axon collateral target density at C1–C2, target density is reduced at T1–T2 by ~30% ($p < 0.01$, unpaired two-tailed t test) and is increased at L1–L2 by ~2-fold ($p < 0.001$; Figures 6D and 6I). Strikingly, neither CSN_{TL} axon collateral target density at T1–T2 nor at L1–L2 is distinguishable between wild-type and *Lumican* null mice (Figure 6I), even though CSN_{TL} axon collaterals at T1–T2 can respond to ectopically overexpressed Lumican (Figure S3C). These findings indicate that Lumican suppresses CSN_{TL} axon collateralization specifically in cervical cord and does not normally regulate CSN_{TL} axon collateralization in thoracic or lumbar cord.

To further investigate whether Lumican regulates initial CSN axon collateralization or later refinement of CSN collateralization, we analyzed CSN_{TL} axon collaterals at P15 after intraperitoneal tamoxifen injection at P3. There is substantial reorganization of CSN axon collaterals after P25 in cats,[58] thought to correspond to around P17 in mice,[59] and after around P14 in mice.[60] We find that CSN_{TL} axon collateral density at C1–C2 and C3–C4 is indistinguishable between wild-type and *Lumican* null mice at P15 (Figures 6J and 6K). This result indicates that initial gray matter entry of CSN_{TL} axon collaterals and their growth

at P15 are unchanged in *Lumican* null mice, before the striking increase observed at P35. Thus, the later increase in CSN_{medial} axon collateral density in *Lumican* null mice is due to deficient corticospinal circuitry refinement, such as reduced collateral pruning, after P15.

Taken together, our results by multiple independent approaches indicate that Lumican is expressed selectively by $CSN_{BC\text{-}lat}$, and suppresses ultimate axon collateralization by both CSN_{TL} and $CSN_{BC\text{-}med}$ in the cervical cord to sculpt circuitry in a non-cell-autonomous manner. The restriction of Lumican function to the cervical spinal cord occurs via its specificity of expression by $CSN_{BC\text{-}lat}$.

Lumican null mice have reduced forelimb dexterity

To investigate functional importance of Lumican-controlled precision in CSN axon collateralization balance within the cervical spinal cord, we pursued a widely used and sensitive measure of forelimb use: a pellet grasping test.[61,62] We first sought to determine via open field testing whether there are gross motor abnormalities, as opposed to finer abnormalities of skilled forelimb movement. There is no difference in either mean velocity or total distance moved between wild-type and *Lumican* null mice in open field testing (Figure 7A), indicating that there are no gross motor abnormalities in *Lumican* null mice. In striking contrast, however, there is a significant impairment in pellet grasping in *Lumican* null mice. While both wild-type and *Lumican* null mice exhibit a similar level of interest, and improve their forelimb usage over the training period, *Lumican* null mice show significantly lower precision in skilled forelimb movement (Figures 7B, 7C, and S7A), indicating that *Lumican* null mice exhibit compromised forelimb dexterity rather than a deficit in motor learning.

To investigate more deeply whether the aberrant refinement of collateralization in *Lumican* null mice causes dysfunction across the range of flexor and extensor muscle groups of the forelimb, as expected, or in a more restricted group of forelimb muscles, we quantified the percentage of failures into well-established categories of reaching, grasping, and retrieving. There is no difference in the error rate distribution among these three categories between wild-type and *Lumican* null mice (Figure S7A), reinforcing the interpretation that optimal collateralization refinement by Lumican is important for motor output from multiple cervical levels. Taken together, these results further reinforce that collateral precision enabled by specific Lumican expression by $CSN_{BC\text{-}lat}$ is critical to overall skilled forelimb use.

We also pursued wide and medium-width balance beam testing (Figure S7B), in which a mouse traverses an elevated beam to assess fine motor coordination and balance.[64] Although there was a modest trend of increase in forelimb slips on the medium-width beam in *Lumican* null mice, it was not statistically significant. *Lumican* null mice do not show any change on either wide or medium-width beams in the number of hindlimb slips or in the time to cross the beam. These results are consistent with the data that CSN_{TL} axon extension and collateralization in thoracic and lumbar segments are normal in *Lumican* null mice (Figures 6G–6I).

Together, these findings indicate that the refined and precise cervical collateralization of CSN enabled by Lumican expression by $CSN_{BC\text{-}lat}$ is required for optimal skilled forelimb movement.

DISCUSSION

In the work presented here, we first identified that the proteoglycan Lumican is expressed exclusively by $CSN_{BC\text{-}lat}$. We further identified that Lumican non-cell-autonomously suppresses axon collateralization by both caudomedial CSN subpopulations, $CSN_{BC\text{-}med}$ and CSN_{TL} (Figure 7D). It is noteworthy that $CSN_{BC\text{-}lat}$, residing outside M1, control development of corticospinal axons arising from M1. Additionally, this suppression occurs independent of any effects on CSN main axon extension, indicating that molecular control over axon collateralization in spinal gray matter is dissociable from control over CSN main axon extension in spinal white matter.[1,65] These results identify a molecularly mediated crosstalk between axons of distinct CSN subpopulations that refines their differential cervical innervation during development and enhances forelimb dexterity. Such mechanisms likely represent a key step in establishing precision of corticospinal circuitry, an axon-projection pathway in which distinct subpopulations likely controlling distinct functional outputs reside in an interdigitated and non-topographic manner. Further, the segmental specificity of corticospinal connectivity serves as an exemplar for regional specificity of many projection neuron connections; thus, these mechanisms might generalize beyond the motor output system.

We speculate that these findings might enable new insights and deeper understanding of how corticospinal circuitry for skilled motor control has evolved in mammals. We recently characterized anatomical and molecular identity of $CSN_{BC\text{-}lat}$ in mice and, through this recent and other work,[22,23,66] it seems likely that this CSN subpopulation is evolutionarily newer. We now identify a mechanism by which this evolutionarily newer subpopulation regulates axon collateralization by evolutionarily older CSN_{medial}. It is intriguing to consider this as a form of “innervation competition”—that evolutionarily newer CSN collateralize and more effectively innervate targets for the finest motor control in the brainstem and cervical cord at least in part by actively suppressing and thus rewiring the connectivity of their evolutionarily older counterparts to less “critical” spinal targets. Notably, while CSN_{medial} axon collaterals primarily respond to Lumican (Figures S3C and S3D), $CSN_{BC\text{-}lat}$ in *Lumican* null mice exhibit a trend toward reduced axon collateralization (Figure 2J), potentially reflecting a secondary effect of relatively increased axon collateralization by CSN_{medial} (Figure 2). The data from our experiments strongly suggest that CSN_{medial} axons have taken up $CSN_{BC\text{-}lat}$ “collateral space” in *Lumican* null mice; CSN_{medial} appear to “compete” more effectively in the absence of Lumican.

Similar or related mechanisms might have likely emerged during mammalian evolution for refinement of corticospinal circuitry. A separate motor cortex emerged in placental mammals about 100 million years ago.[19] Non-primate early mammals then acquired additional motor areas, such as dorsal premotor and supplementary motor areas.[20] Interestingly, ventral premotor area is considered unique in primates.[20] Importantly, all these areas that appeared more recently through evolution also display cervical corticospinal

innervation in primates, suggesting the potential for inter-axonal crosstalk between these distinct corticospinal projections.[8,9]

Remarkably, expression analyses in the developing primate cortex reveal that SLRPs, including Lumican, are expressed in appropriate locations, and at appropriate developmental times, potentially controlling corticospinal axon branching during development. Developing marmoset cortex at birth, whose neural development corresponds roughly to P10 in mice,[59] exhibits similar, but expanded, *Lumican* expression (Figure 7E).[63,67] Even more strikingly, another SLRP family member, *Decorin*, shows prominent layer V expression in ventrolateral cortex in marmosets (Figures 7E),[63,67] but not in mice (Figures 7F and 7G).[22] Expanded use of SLRPs might underlie evolutionary rewiring of corticospinal circuitry, which could potentially underlie refinement of motor control.

Lumican regulates CSN axons at sites remote from their parental soma in a paracrine fashion, perhaps by binding to secreted non-structural molecules (Figure S4). Axon guidance is classically mediated via both attractive and repulsive cues from intermediate or final targets and via axon-axon interactions.[1,2,33,68,69] Intriguingly, Lumican suppresses axon collateralization by other populations of neurons without altering the trajectory of the main CST.

Our findings suggest that Lumican controls refinement of CSN innervation, after an initial period of overabundant innervation. This reorganization takes place after P15 (Figures 6J and 6K), whereas Lumican protein expression in $CSN_{BC\text{-}lat}$ cell bodies appears to peak by P15 (see Figures 1B–1E and S1B–S1D). We speculate that Lumican protein trafficking in and secretion from CSN axons is temporally controlled and/or that Lumican downstream mechanisms take a long time to exert their function(s). It will be interesting to investigate if Lumican works together with neural activity and caspase pathways, which have been shown to regulate the reorganization of CSN axon collaterals.[60] Lumican function identified here will help elucidate how axons with similar identities establish and maintain distinct target innervation and likely mediate distinct circuit function(s).

The relevance of initial development of connectivity and circuitry both for later disease vulnerability and for plasticity is supported by increasingly emerging evidence. It appears increasingly likely that subtle perturbations of early, circuit-specific developmental controls can lead to formation of subtly altered circuitry that is more vulnerable to disease in later life, whether by primary dysfunction or by less effective maintenance. Intriguingly, a unique, non-synonymous *Lumican* variant was reported in a patient cohort of amyotrophic lateral sclerosis,[70] a disease characterized by progressive degeneration of CSN and spinal motor neurons.[71,72] Further, *Lumican* is reported to be upregulated upon pyramidotomy in adult rat cervical cord.[73] It is interesting to consider whether Lumican manipulation after CST injury might enable rewiring with greater precision for enhanced recovery.[73–77]

CSN exhibit substantial targeting and circuit diversity and likely have even much greater molecular and functional diversity than described here, considering the tremendous areal, segmental, functional, and evolutionary diversity in the brainstem and spinal cord. Recent advances in single-cell and subcellular sequencing and proteomic technologies will enable

further identification of CSN heterogeneity.[78–82] Identifying specific somatic and subcellular gene expression, RNA and protein localization, and local translational regulation signatures of increasingly more specific CSN subpopulations will enable molecular manipulations and circuit analyses of increasingly more specific circuit- and functionally defined subsets of CSN. Elucidating dynamic, subtype-specific RNA and protein molecular machinery in subtype-specific growth cones *in vivo*,[80] as well as postsynaptic target cell identity[17] of progressively more delineated CSN subpopulations, will contribute substantially to parsing and understanding corticospinal circuitry development, function, and evolution of seemingly "layered," increasingly precise and advanced function-specific neuron populations. It is also possible that Lumican might regulate other descending pathways either directly or indirectly, including rubrospinal and reticulospinal pathways, as well as local circuits in the spinal cord. Future investigation will progressively deepen the understanding of corticospinal development, functional organization, evolution, and selective vulnerability to degeneration, which together might enlighten and enable novel approaches for circuit regeneration and repair.

Limitations of the study

We present here three limitations. First, as noted above, our attempts to identify specific receptor-dependent signaling and/or multipartite binding partners did not optimally elucidate a molecular mechanism(s) downstream of Lumican. Although our IP-MS experiments suggest potential Lumican interactions with partner proteins, a central mechanistic limitation of this study is the continued lack of clarity regarding how Lumican controls inter-axonal crosstalk between CSN subpopulations at the molecular mechanistic level. Toward such further elucidation, we provide for the field all our raw data from ultra-low-input proteomics. Second, given the exquisitely specific expression of Lumican, we reasoned that investigating *Lumican* null mice would achieve the goals most typically achieved using conditional mutant mice. Further, we investigated Lumican functions by directly manipulating Lumican expression within specific corticospinal subpopulations—both where it is normally expressed and in subpopulations that normally do not express Lumican —and also in cervical spinal cord. That said, additional insight might be gained by using conditional *Lumican* mutant mice, which might provide even more defined cell-type specificity and temporal control over Lumican loss of function. Third, our early comparative expression results and speculations regarding corticospinal circuitry evolution warrant further direct experimental investigation in multiple mammalian species that vary in corticospinal organization and circuitry.

STAR★METHODS

RESOURCE AVAILABILITY

Lead contact—Further information and requests for resources and reagents should be directed to and will be fulfilled by the lead contact, Dr. Jeffrey D. Macklis (jeffrey_macklis@harvard.edu).

Materials availability—All unique/stable reagents generated in this study are available with a material transfer agreement from the lead contact for academic, non-commercial

use; negotiation and completion of a material transfer agreement with Harvard University is required if there is potential for commercial application.

Data and code availability

- Lumican and Mfge8 IP-MS data have been deposited at Harvard Dataverse repository and are publicly available. The DOIs are listed in the key resources table. Microscopy data reported in this paper will be shared by the lead contact upon request.
- This paper does not report original code.
- Any additional information required to reanalyze the data reported in this paper is available from the lead contact upon request.

EXPERIMENTAL MODEL AND SUBJECT DETAILS

Mice used in this study—All mouse studies were approved by the Harvard University IACUC, and were performed in accordance with institutional and federal guidelines. The day of birth was designated as P0. The genders of early postnatal mice were not determined. Mice of both sexes were used in this study. Mice were used at the following ages: P4, P5, P7–P10, P13–P15, 3–6 weeks old, and 7–20 weeks old. Mice were group housed with light on a 12:12 or 14:10 h cycle. Water and food were provided *ad libitum*.

Wild-type mice on a C57BL/6J or CD1 background were obtained from Charles River Laboratories (Wilmington, MA). *Lumican*$^{+/-}$ mice were generously provided by Dr. Shukti Chakravarti.[47] All *Lumican*$^{+/-}$ mice used in this study were maintained on a CD1 or CD1/C57BL/6J mixed background. *Fezf2*$^{-/-}$ and *Emx1*$^{IRES\text{-}Cre/IRES\text{-}Cre}$ mice were generated previously.[86,87] *Crim1*$^{GCE/+}$ mice were obtained from Jackson Laboratories.[22,23] CreERT2 activity was induced at P3 by intraperitoneally injecting 50 μL of Tamoxifen (Sigma, T5648) solution dissolved in corn oil (Sigma, C8267) at 8 mg/mL. *Emx1*$^{IRES\text{-}FlpO/IRES\text{-}FlpO}$ mice were generated previously.[22] *Ai65*$^{RCFL\text{-}tdT/RCFL\text{-}tdT}$ mice were obtained from Jackson Laboratories, and genotyped using their recommended protocol.

Primary cortical neuron culture—P0 wild-type mouse brains were dissected out, and cortices were dissociated to obtain single cell suspensions.[88] Cortices were dissected in ice-cold dissociation medium (20 mM glucose, 0.8 mM kynurenic acid, 0.05 mM DL-2-amino-5-phosphonopentanoic acid (APV), 50 U/mL penicillin–0.05 mg/mL streptomycin, 0.09 M Na_2SO_4, 0.03 M K_2SO_4 and 0.014 M $MgCl_2$; pH 7.35 ± 0.02), and enzymatically digested in dissociation medium containing 0.16 mg/L L-cysteine HCl, 10 U/mL papain (Worthington, Lakewood, NJ), and 20 U/mL DNase (pH 7.35 ± 0.02) at 37°C for 15–20 min, followed by rinsing with dissociation medium containing OVO/BSA (pH 7.35 ± 0.02) at RT to inhibit the papain, and finally washed with ice-cold OptiMEM (GIBCO, Life Technologies, Gaithersburg, MD) containing 20 mM glucose and both 0.4 mM kynurenic acid and 0.025 mM APV to protect against glutamate-induced neurotoxicity. Cortices were mechanically dissociated by gentle trituration, and single cortical neurons were resuspended. Dissociated neurons were nucleofected with pAAV-EGFP-2A-Stop or pAAV-EGFP-2A-Lumican plasmid, using an Amaxa Mouse Neuron Nucleofector kit (Lonza,

VPG-1001),[88] and were cultured at 37°C with 5% CO_2 for 7 hours in Neurobasal Medium (Gibco, 21103049) supplemented with 5% fetal bovine serum (VWR, 97068–085), 0.25% GlutaMAX (Gibco, 35050061), 2% B27 (Invitrogen, 17504044), and 0.6% glucose (Sigma, G6152), then for 7 days in Neurobasal Medium (Gibco, 21103049) supplemented with 1% GlutaMAX (Gibco, 35050061) and 2% B27 (Invitrogen, 17504044) on poly-D-lysine–coated 6 well plates. The genders of P0 mice were not determined.

Cell culture—HEK 293T cells were cultured at 37°C with 5% CO_2 in Dulbecco's modified Eagle medium (Gibco, 10566024) supplemented with 10% (v/v) fetal bovine serum, 100 U/mL penicillin, and 100 μg/mL streptomycin (Thermo Scientific, 15140122).

METHOD DETAILS

DNA constructs—To generate pAAV-EGFP-2A-Stop (in which a stop codon was placed in frame 3′ to the EGFP coding sequence), the *EGFP-2A-Stop* coding sequence was cloned into an AAV shuttle plasmid (obtained from the Massachusetts General Hospital Virus Core) that contains the following elements flanked by AAV2 ITRs: a CMV/β-actin promoter to drive the expression of the gene of interest, followed by the woodchuck hepatitis virus post-transcriptional regulatory element (WPRE), an SV40 polyadenylation signal, and a bovine growth hormone polyadenylation signal. Mouse *Lumican* cDNA (Open Biosystems, 3585672) was inserted 3′ to the *EGFP* coding sequence; the two ORFs were separated by a T2A linker sequence in-frame to create a bicistronic expression vector pAAV-EGFP-2A-Lumican. A vector expressing fusion protein of the FLRT3 ectodomain and Fc domain of human IGHG1 (FLRT3-Fc) was provided by D. Comoletti. Nucleotides encoding the FLRT3 ectodomain were excised to generate a vector expressing only the Fc domain, or were replaced by mouse *Lumican* cDNA to generate a Lumican-Fc–expressing plasmid. Expression plasmids or cDNAs for genes listed in Figure S4A were provided by E. Kim, A. Ghosh, J. de Wit, G. Miyoshi, A. Poulopoulos, or Y. Mukouyama, purchased from Addgene or Sino Biological, or generated previously.[23]

Retrograde labeling by CTB—Developmental CSN at P4 were retrogradely labeled bilaterally from cervical or thoracic spinal cord by injecting 161 nL of the retrograde label cholera toxin B subunit (CTB) conjugated to Alexa 647 (CTB-647, 1 mg/mL in phosphate buffer saline (PBS); Thermo Scientific, C34778) into each side of the midline guided by ultrasound backscatter microscopy (VisualSonics, Vevo 3100) via a pulled glass micropipette (Drummond Scientific, 3–000-203-G/X) with a digitally-controlled, volume-displacement nanojector (Nanoject II, Drummond Scientific). For these neonatal injections, pups were anesthetized under ice for 4 minutes. After injections, the pups were placed on a heating pad at 37°C for recovery. Pups were perfused for Lumican immunocytochemical analysis at P5.

CSN at P35 were retrogradely labeled bilaterally from cervical C1 segment by CTB-555 (2 mg/mL in PBS; Thermo Scientific, C22843). For these adult injections, mice were anesthetized under isoflurane. After laminectomy at the C1 vertebral segment, 322 nL of CTB-555 solution was injected into each side of the midline via a pulled glass micropipette with a Nanoject II. The skin was then sutured, and mice were placed on a heating pad at

37°C for recovery. Mice were subsequently perfused at P42 for analysis of CTB-labeled CSN in cortex.

Preparation of AAV particles—AAV2/1 particles for AAV-EGFP and AAV-EGFP-2A-Lumican expression were generated at the Massachusetts General Hospital Virus Core using established protocols.[83] AAV8 hSyn-EGFP-Cre (described as "AAV-hSyn-EGFP-Cre") was obtained from the vector core at the University of North Carolina at Chapel Hill. AAV Retrograde pmSyn1-EBFP-Cre (described as "AAV-retro-Cre") and AAV1 pCAG-Flex-tdTomato-WPRE (described as "AAV-CAG-FLEX-tdTomato") were obtained from Addgene. AAV1.hSyn.TurboRFP.WPRE.rBG (described as "AAV-hSyn-turboRFP") and AAV1.CAG.Flex.eGFP.WPRE.bGH (described as "AAV-CAG-FLEX-EGFP") were obtained from the vector core at the University of Pennsylvania.

All virus work was approved by the Harvard Committee on Microbiological Safety, and conducted according to institutional guidelines.

Anterograde and retrograde labeling with AAV in early postnatal pups—For anterograde labeling of cortical neurons via AAV-mediated gene delivery, P1, P2, or P4 pups were anesthetized using hypothermia, for which pups were placed under ice for 2–4 minutes. The cortex was visualized via ultrasound backscatter microscopy (VisualSonics, Vevo 770 and 3100), then injected using a pulled glass micropipette attached to Nanoject II digitally-controlled volume injection system. The shapes of the brain, lateral ventricle, and hippocampus, along with skull surface markers, served as landmarks for these intracranial injections. For retrograde CSN labeling by AAV injection into the spinal cord, pups were similarly anesthetized, and the spinal cord was visualized using ultrasound backscatter microscopy. For these intraspinal (dorsal funiculus) injections, the size and shape of spinal segments, along with the midline, served as reproducible landmarks. After injections using the Nanoject II, pups were placed on a heating pad for recovery. CTB-647 (0.1 mg/mL; Invitrogen, C34778) was mixed with AAV-retro-Cre solution to visualize the injection sites in the spinal cord.

AAV titers and volumes used: AAV-EGFP, 9.4×10^{12} GC/mL, 115 nL (unilateral, Figure S3F) or 161 nL (Figures 4 and S3A), and 3.6×10^{12} GC/mL, 230 nL (Figures S3C and S3D); AAV-EGFP-2A-Lumican, 3.6×10^{12} GC/mL, 115 nL (unilateral, Figure S3F) or 230 nL (Figures 4 and S3A–S3E); AAV-retro-Cre, 5.4×10^{12} GC/mL, 115 nL (bilateral, Figures 5 and S5); AAV1-CAG-FLEX-tdTomato, 7.7×10^{12} GC/mL, 46 nL (Figure S3F); AAV-hSyn-EGFP-Cre, 8.1×10^{11} GC/mL, 46 nL (Figure S3F).

Anterograde labeling by tracer and AAV injections into juvenile (4-week-old) mice—To anterogradely label CSN in caudomedial sensorimotor cortex, we used 10,000 Da lysine-fixable biotinylated dextran-amine (BDA; Invitrogen, D1956), iontophoretically delivered into the appropriate cortical location. A small craniotomy was made over the left hemisphere of anesthetized 4-week-old mice positioned in a stereotactic frame (Stoelting). A pulled glass micropipette (~80-μm–inner diameter tip) loaded with a 10% solution of BDA in PBS was stereotactically positioned at the following coordinates; anterior-posterior (AP) ± 0 mm; medio-lateral (ML) +1.0 mm; dorsoventral (DV) +0.8 mm from pia. Using an

Isolated Pulse Stimulator (A-M Systems, Model 2100), intermittent pulses of 8 μA current were delivered for 7 seconds, with an inter-pulse interval of 7 seconds, for a total duration of 20 min. The skin was sutured, and mice were placed on a heat pad for recovery. Mice were perfused 7 days later for subsequent analysis.

To anterogradely label CSN via AAV-mediated gene delivery, we performed unilateral AAV microinjections into the appropriate location in sensorimotor cortex. A small craniotomy was performed over the left hemisphere of anesthetized 4-week-old mice positioned in a stereotactic frame, and a pulled glass micropipette loaded with AAV was stereotactically positioned at the following coordinates: For rostrolateral sensorimotor cortex injection, AP +1.5 mm; ML +3.0 mm; DV +1.0 mm from pia; for caudomedial sensorimotor cortex injection, see above. Following injection of AAV particles, the skin was sutured, and mice were placed on a heat pad to recover. Mice were perfused 14 days later for cytochemical analysis.

An intersectional viral labeling approach was used for exclusionary, subtractive labeling of the two CSN subpopulations within caudomedial sensorimotor cortex ($CSN_{BC\text{-}med}$ and CSN_{TL}). This approach takes advantage of both the location of $CSN_{BC\text{-}med}$ in caudomedial sensorimotor cortex, and the segmental projection of $CSN_{BC\text{-}med}$ axons extending only to bulbar-cervical segments. When injected into caudomedial sensorimotor cortex, an AAV-expressed reporter under control of pan-neuronal promoter will label all neurons, including both CSN_{TL} and $CSN_{BC\text{-}med}$, while a conditional, Cre-dependent AAV-expressed reporter combined with retrogradely transported AAV-Cre (AAV-retro-Cre[89]) injected into the thoracic cord will label only CSN_{TL}, and not $CSN_{BC\text{-}med}$. The combination of these two strategies enables delineation of $CSN_{BC\text{-}med}$ as a specific subset within the spatially defined overall population of CSN_{medial}. AAV-retro-Cre was first injected into thoracic T3–T4 in wild-type and *Lumican* null mice at P4. A Cre-dependent AAV-CAG-FLEX-EGFP along with AAV encoding turboRFP under the control of human *Synapsin 1* promoter (AAV-hSyn-turboRFP) were then co-injected into caudomedial sensorimotor cortex in 4-week-old mice.

AAV titers and volumes used: AAV-hSyn-turboRFP, 9.6×10^{12} GC/mL (Figures 5 and S5), 92 nL; AAV-CAG-FLEX-EGFP, 2.3×10^{13} GC/mL, 92 nL (Figures 5 and S5); AAV-CAG-FLEX-tdTomato, 7.7×10^{12} GC/mL, 230 nL (Figure 2J); AAV-hSyn-EGFP-Cre, 8.1×10^{11} GC/mL, 230 nL (Figure 2J).

Immunocytochemistry and *in situ* hybridization—Mice were transcardially perfused with cold PBS followed by 4% paraformaldehyde (PFA) in PBS, and brains and spinal cords were dissected and postfixed in 4% PFA/PBS at 4°C overnight. Spinal cords were sectioned on a cryostat (Leica, CM 3050S) at 50 μm (all figures except Figures 6B–6I or S3E) or 70 μm (Figures 6B–6I), or on a vibrating microtome (Leica) at 50 μm (Figure S3E). Brain sections were collected on a cryostat at 50 μm thickness. Non-specific binding was blocked by incubating tissue and antibodies in 2% donkey serum (Millipore, S30–100ML)/ 0.3% BSA (Sigma, A3059–100G) in PBS with 0.3% Triton X-100 or 0.3% BSA in PBS with 0.3% Triton X-100. In most instances, tissue sections were incubated with primary antibodies at 4°C overnight. Thicker sections (70 μm) of the spinal cord were incubated with primary antibodies at 4°C for 2 days. Secondary antibodies were chosen from the

Alexa series (Invitrogen), and used at a dilution of 1:500 for 3–4 hours at room temperature (RT). For DAPI staining, tissue was mounted in DAPI-Fluoromount-G (SouthernBiotech, 0100–20).

Primary antibodies and dilutions used: goat anti-Lumican (R&D Systems, AF2745, 1:200); goat anti-Decorin (R&D Systems, AF1060, 1:200); rabbit anti-Lumican (Abcam, ab168348, 1:100); mouse anti-PECAM-1 (Cell Signaling, 3528S, 1:500); rat anti-CTIP2 (Abcam, ab18465, 1:2,000); mouse anti-SATB2 (Abcam, ab51502, 1:500); rabbit anti-TBR1 (Abcam, ab31940, 1:500); rabbit anti-GFP (Invitrogen, A11122, 1:1,000); rabbit anti-RFP (Rockland, 600–401-379, 1:500). For Lumican staining in Figure S3B, sections were incubated in 0.1 M citric acid, pH 6.0, for 5 min at 95–98°C for antigen retrieval prior to standard staining protocol.

BDA was visualized using an ABC-HRP kit (VECTOR laboratories, PK-4000) and 3,3′-Diaminobenzidine (Sigma, D4418). After mounting on gelatin-coated glass slides, sections were dehydrated in ethanol, cleared in xylene, and mounted in DPX mountant (Sigma, 06522).

In situ hybridization was performed using an established protocol.[22,23] Briefly, 14 or 50 μm thick cryosections mounted on glass slides (VWR, 48311–703) were hybridized with a probe labeled by digoxigenin, followed by incubation with anti-digoxigenin antibody conjugated to alkaline phosphatase. Sections were developed in a substrate solution containing 5-bromo-4-chloro-indolylphosphate and nitroblue tetrazolium chloride. The 3′ untranslated region of *Lumican* cDNA (nucleotides 1517 to 2004, NM_008524) was used as a probe. See ref. 22 for *Klhl14, Cartpt, Cry-mu, and Crim1* probes.

Single molecule *in situ* hybridization was performed using the RNAscope 2.5 HD RED kit according to the manufacturer's instructions (Advanced Cell Diagnostics). In brief, 16 μm thick axial cryosections of cervical and lumbar segments were mounted onto glass slides in phosphate buffer (pH 7.2), airdried, and baked at 60°C for 30 min, followed by pretreatment with hydrogen peroxide for 10 min, target retrieval, and ethanol dehydration. After the pretreatment with Protease Plus (1:10 diluted in PBS) at 40°C for 30 min, sections were incubated with *Lumican* probe (480361, Entrez Gene: NM_008524.2) at 40°C for 2 h, and the standard RNA-scope protocol was followed. Incubation time of amplification step 5 and color reaction were optimized at 15 min and 7.5 min, respectively.

Immunoblot analysis—Tissues were microdissected, and the meningeal membrane was removed from both rostrolateral sensorimotor cortex and spinal cord. Microdissected tissue was lysed in a buffer containing 50 mM Tris-HCl (pH 7.5), 150 mM NaCl, 1.0% Triton X-100, 1 mM dithiothreitol, 1 mM EDTA, and Halt inhibitor cocktail (Thermo Scientific, 78440). Lysates were centrifuged at 20,000 *g* at 4°C for 15 min, and the resulting supernatants were analyzed.

Primary cortical neurons were washed with PBS, and lysed with a cell lysis buffer containing 20 mM Tris-HCl (pH 7.5), 150 mM NaCl, 10 mM β-glycerophosphate, 5 mM EGTA, 1 mM $Na_4P_2O_7$, 5 mM NaF, 0.5% Triton X-100, 1 mM Na_3VO_4, 1 mM

dithiothreitol, 1 μg/mL aprotinin, and 1 μg/mL leupeptin. The lysate was centrifuged at 20,000 *g* at 4°C for 15 min to separate supernatant (soluble fraction) and pellet (insoluble fraction containing nuclei). Conditioned medium was centrifuged at 960 g at 4°C for 10 min, and the resulting supernatant was further centrifuged at 20,000 g at 4°C for 10 min to remove debris (Figure S1L).

Following standard Tris-glycine SDS–PAGE, resolved proteins were electroblotted onto PVDF membranes using semi-dry transfer. Ponceau S was used for staining the total protein transferred to the membrane. Membranes were incubated with primary antibodies diluted in 5% BSA in TBS with 0.1% Tween 20 or in Can Get Signal buffer (Toyobo, NKB-201). The following primary antibodies were used for immunoblotting: mouse anti-β-actin (Sigma, A5441, 1:5,000); mouse anti-PECAM-1 (Cell Signaling Technology, 3528S, 1:500); rabbit anti-GFP (Invitrogen, A11122, 1:1,000); goat anti-Lumican (R&D Systems, AF2745, 1:200). HRP-conjugated secondary antibodies (Abcam, ab98693 and ab6721; Santa Cruz, sc-2020) were used for ECL imaging. Immunoreactive bands were detected by chemiluminescence using SuperSignal West Pico PLUS (Thermo Scientific, 34580), which was visualized using a CCD camera imager (FluoroChemM, Protein Simple). Fiji[90] was used to measure band intensities.

HEK 293T cell surface binding assay—HEK 293T cells were transfected with constructs encoding a candidate transmembrane protein of interest, Lumican, or Fc-fusion protein as shown in Figures S4A–S4C using FuGene 6 (Promega). Two days after transfection, cells expressing the transmembrane protein were incubated with conditioned medium obtained from cells expressing Lumican or the Fc-fusion protein for 1 hour at RT. Cells were then fixed and immunolabeled using goat anti-Lumican (R&D Systems, AF2745, 1:200) and donkey anti-goat IgG Alexa555 (Invitrogen, A-21432, 1:500) for Lumican detection, or using goat anti-human IgG Alexa555 (Invitrogen, A-21433, 1:500) for Fc detection. Mouse anti-myc 9E10 (Sigma, M4439, 1:1,000) was used for labeling Myc-Ntng1/2. Non-specific binding was blocked by incubating cells and antibodies in 2% donkey serum/0.3% BSA in PBS with 0.3% Triton X-100. For DAPI staining, cells were mounted in DAPI-Fluoromount-G.

Section binding assay—HEK 293T cells were transfected with constructs encoding Fc, Lumican-Fc, or FLRT3-Fc using FuGene 6. Cells were washed with PBS after 1–2 days, and were further incubated in Opti-MEM (Gibco, 51985034) for 1–3 days. After this incubation period, conditioned medium was diluted with Opti-MEM (as indicated in Figure S4D) before application onto tissue sections. The presence of secreted Fc Fusion protein in the medium was confirmed by immunoblotting with goat anti-human IgG antibody (Invitrogen, A-21433, 1:500).

Following euthanasia, P10 *Lumican* null mice were immediately perfused with cold PBS, followed by brain and cervical cord dissection. The microdissected tissues were fresh frozen in liquid nitrogen, then embedded in OCT compound (Sakura Finetek). Twelve μm thick coronal brain sections and axial cervical sections obtained on a cryostat were mounted on glass slides (VWR, 48311–703), and treated as described.[55] Briefly, sections were immediately postfixed in precooled methanol at 20°C for 7 min, washed twice with

PBS, blocked with PBS containing 10% fetal bovine serum (VWR, 97068–085) for 15 min, and incubated with Opti-MEM conditioned medium described above for 1 hour at RT. Then, sections were fixed in 4% PFA/PBS for 5 min at RT, washed three times with PBS, and incubated with goat anti-human IgG Alexa555 (Invitrogen, A-21433, 1:500) in 0.3% BSA/PBS for 30 min at RT. Sections were then washed three times with PBS, and mounted in DAPI-Fluoromount-G.

Immunoprecipitation and mass spectrometry—In Lumican IP-MS experiments, cervical spinal cords were dissected from P7-P10 wild-type mice, *Lumican* null mice, or *Lumican* null mice that received AAV-EGFP-2A-Lumican (3.6×10^{12} GC/mL, 115 nL each, bilateral) injection into primary motor cortex at P1. Meninges were carefully removed during dissection. Tissue was homogenized with a Dounce homogenizer in a buffer containing 50 mM Tris-HCl (pH 7.5), 150 mM NaCl, 1.0% Triton X-100, 1 mM dithiothreitol, 1 mM EDTA, and Halt inhibitor cocktail. The lysates were incubated for 10 min on ice, followed by a 15 min centrifugation at 21,000 × g, 4°C. The supernatant was incubated with 2.5 μg of goat anti-Lumican antibody (R&D Systems, AF2745) for 2–4 h at 4°C, followed by incubation with 12.5 μL Dynabeads Protein G solution (Thermo Fischer) for 30 min at 4°C. Then, the beads-antibody-protein complexes were washed 3 times with PBS.

In Mfge8 IP-MS experiments, cervical spinal cords were dissected from P10 wild-type mice. Meninges were carefully removed during dissection. Tissue was homogenized with a Dounce homogenizer in a buffer containing 50 mM Tris-HCl (pH 7.5), 150 mM NaCl, 1.0% Triton X-100, 1 mM dithiothreitol, 1 mM EDTA, and Halt inhibitor cocktail. The lysates were incubated for 10 min on ice, followed by a 15 min centrifugation at 21,000 × g, 4°C. The supernatant was incubated with 2.5 μg of goat anti-Mfge8 antibody (R&D Systems, AF2805) or control goat antibody (R&D Systems, AB-108-C) for 2–4 h at 4°C, followed by incubation with 12.5 μL Dynabeads Protein G solution (Thermo Fischer) for 30 min at 4°C. Then, the beads-antibody-protein complexes were washed 3 times with PBS.

Proteomic analysis was performed at the Harvard Center for Mass Spectrometry. The beads-antibody complexes were resuspended in 100 μL Triethylammonium bicarbonate buffer and heated at 95°C for 5 min, followed by Trypsin/Lys-C treatment (Promega; 1:50) at 37°C for 3 hours. The samples were them submitted for LC-MS/MS experiment that was performed on a Orbitrap Lumos (Thermo Fischer, San Jose, CA) equipped with dual pump Ultimate 3000 nanoLC (Thermo Fischer, San Jose, CA). Peptides were separated onto a 100 μm inner diameter microcapillary trapping column packed first with approximately 5 cm of C18 Reprosil resin (5 μm, 100 Å, Dr. Maisch GmbH, Germany) followed by analytical column μPAC Column 50cm by PharmaFluidics (ESI Source Solutions). Separation was achieved through applying a gradient from 5–27% acetonitrile in 0.1% formic acid over 90 min at 200 nL/min. Electrospray ionization was enabled through applying a voltage of 1.8 kV using a home-made electrode junction at the end of the microcapillary column and sprayed from fused silica pico tips (New Objective, MA). The LTQ Orbitrap Lumos was operated in data-dependent mode for the mass spectrometry methods. The mass spectrometry survey scan was performed in the Orbitrap in the range of 395–1,800 m/z at a resolution of 6 × 104, followed by the selection of the thirty most intense ions (TOP30)

for collision-induced dissociation (CID)-MS2 fragmentation in the Ion trap using a precursor isolation width window of 2 m/z, automatic gain control (AGC) setting of 10,000, and a maximum ion accumulation of 200 ms. Singly charged ion species were not subjected to CID fragmentation. Normalized collision energy was set to 35 V and an activation time of 10 ms. Ions in a 10 ppm m/z window around ions selected for MS2 were excluded from further selection for fragmentation for 60 s.

Mass spectrometry analysis: Raw data were submitted for analysis in Proteome Discoverer 2.4 (Thermo Scientific) software. Assignment of MS/MS spectra was performed using the Sequest HT algorithm by searching the data against a protein sequence database including all entries from our Uniprot_HUMAN_SPonly_2018.fasta database as well as other known contaminants such as human keratins and common lab contaminants. Sequest HT searches were performed using a 20 ppm precursor ion tolerance and requiring each peptides N-/C termini to adhere with Trypsin protease specificity, while allowing up to two missed cleavages. Peptide N termini and lysine residues (+229.162932 Da) was set as static modifications while methionine oxidation (+15.99492 Da) was set as variable modification. A MS2 spectra assignment false discovery rate (FDR) of 1% on both protein and peptide level was achieved by applying the target-decoy database search. Filtering was performed using a Percolator (64bit version). Protein data were analyzed with the DEP package.[91] We retained proteins that were identified in at least two samples for at least one condition, performed variance stabilizing normalization, imputed missing values with a quantile regression-based left-censored function, and tested for differential expression.

Imaging and quantification—For epifluorescence microscopy, tissue sections and cells were imaged using either a Nikon Eclipse 90i or NiE microscope (Nikon Instruments) with a mounted CCD or sCMOS camera (ANDOR Technology), respectively. Z stacks were collapsed using the “Extended Depth of Focus” function on the NIS-Elements acquisition software (Nikon Instruments). Images were processed using ImageJ software (NIH), Fiji, or Adobe Photoshop. For confocal imaging, samples were imaged on an LSM 880 (Zeiss).

To quantify retrogradely labeled CSN distributed in medial versus lateral locations in postnatal cortex, images of 2 coronal brain sections at specific rostral levels 300 μm apart were divided into 5 medio-lateral bins spanning the width of one cortical hemisphere, and medial versus lateral distinction was achieved by combining the 2 medial bins as medial, and the 3 lateral bins as lateral for CSN counts. The medial 2 bins approximately match M1 and M2 areas. One cortical hemisphere was analyzed for each mouse, and every labeled neuron was manually counted in each section using the Cell Counter function in Fiji. To quantify retrogradely labeled CSN distributed in medio-lateral and rostro-caudal locations in adult cortex, 5 matched rostro-caudal coronal brain sections of both cortical hemispheres were analyzed. Each cortical hemisphere was divided into 5 medio-lateral bins, and the 2 medial and 3 lateral bins were combined, respectively, as medial vs. lateral for CSN counts.

To quantify BDA-labeled CST axons at cervical C1–C2, the dorsal funiculus was imaged in axial sections of the cervical spinal cord using a 40× oil immersion objective on the 90i. These Z-stacks were imported into ImageJ, and each labeled axon was manually counted using the entire series of images within each Z-stack. To quantify BDA-labeled

CSN axon collaterals from cervical C3–C8, horizontal sections of the cervical spinal cord were imaged using a 10× objective on the 90i. BDA tracing results shown in Figures 2F–2H and S2C were performed manually using Adobe Photoshop. Individual traced images of serial horizontal sections of spinal cord that contained any axon collaterals were then overlaid using the midline and tissue edges as landmarks. We present the collapsed stack of these tracings in Figure 2H to clearly illustrate the loss-of-function phenotype of *Lumican* null mice. In contrast, the gain-of-function phenotype of Lumican overexpression on axon collateral density reduction is far more pronounced (Figure 4), and readily apparent even on single horizontal sections. Therefore, we did not generate a collapsed stack, since a single section clearly presents the result.

BDA collaterals in the cervical gray matter were also semi-automatedly traced and quantified using ImageJ, using modifications of a previously reported method.[92] Briefly, the largest Hessian with the smoothing scale 2 was applied to images before a threshold was applied. Then, pixels above the threshold were measured to quantify the total area of BDA-positive axon collaterals. After combining tracing results across all horizontal sections spanning the entire cervical gray matter, the resulting total area of BDA-positive axon collaterals was normalized to CST axon number at C1–C2 to calculate relative density of BDA-positive axon collaterals. Both manual and semi-automated tracing approaches gave similar quantification results, validating the semi-automated tracing approach.

To investigate CST axon extension in the spinal cord (Figure 3D), tdTomato fluorescence intensity in the dorsal funiculus labeled by $Emx1^{IRES\text{-}Cre/IRES\text{-}Flpo};Ai65^{RCFL\text{-}tdT/+}$ was measured in axial sections at distinct spinal levels (cervical C1–C2, thoracic T1–T2, and lumbar L1–L2) using Fiji.

Density of axon collaterals labeled by tdTomato (in *Lumican* wild-type; $Crim1^{GCE/+};Emx1^{IRES\text{-}Flpo/IRES\text{-}Flpo};Ai65^{RCFL\text{-}tdT/RCFL\text{-}tdT}$ or *Lumican* null; $Crim1^{GCE/+};Emx1^{IRES\text{-}Flpo/IRES\text{-}Flpo};Ai65^{RCFL\text{-}tdT/RCFL\text{-}tdT}$ mice, or mice injected with tdTomato-expressing AAV) was quantified by first measuring the number of CST axons in the dorsal funiculus at cervical C1–C2, T1–T2, and L1–L2 using axial sections. To quantify the number of CST axons consistently and reproducibly using criteria established *a priori*, a threshold was applied to confocal images (40× or 63× objective) obtained from C1–C2, T1–T2, and L1–L2 axial sections, and the number of axon cross-sections, seen as bright spots of appropriate size on the axial sections, was measured to obtain an estimate of the number of labeled tdTomato$^+$ CST axons. Then, axial sections of the spinal cord were imaged using a 10X objective on the NiE, and the total area of axon collaterals in the gray matter was measured using the semi-automated tracing approach described above (using Fiji).[92] The smallest Hessian with the smoothing scale 0.55 was applied to images obtained from axial sections before a threshold was applied. Then, pixels above threshold were quantified as the total area of tdTomato-positive axon collaterals, then normalized to CST axon number at C1–C2, T1–T2, or L1–L2 to calculate relative density of tdTomato-positive axon collaterals in the gray matter. To quantify the distribution of axon collateralization, entire axial sections from each spinal cord at cervical C3–C4 were divided using Fiji into 600 bins medio-laterally (300 bins in each spinal hemicord) and 400 bins dorso-ventrally. Each bin corresponds to 3.2 μm in width medio-laterally and in height dorso-ventrally.

An intersectional AAV labeling approach was used to specifically label $CSN_{BC\text{-}med}$ (Figures 5 and S5), by labeling neurons and their axons with three patterns of fluorescent protein expression, as shown in Figure 5B. In order to specifically analyze axons labeled only by turboRFP, Fiji was used to subtract $EGFP^+$ pixels from the corresponding turboRFP image, thereby identifying axons with only turboRFP signal (see Figures $5C_{1–4}$ and $5D_{1–4}$). To count CST axons in the dorsal funiculus, a similar subtractive approach was used, by which $EGFP^+$ pixels were first subtracted from the corresponding turboRFP confocal image (63× objective) obtained from C1–C2 axial sections. Then, a threshold was applied to both EGFP and the resulting turboRFP images, followed by particle measurement of bright spots of appropriate size to obtain an estimate of the number of $EGFP^+$ and $turboRFP^+$:$EGFP^-$ CST axons, respectively. To quantify the total area of axon collaterals, the smallest Hessian with the smoothing scale 0.55 was applied to both EGFP and turboRFP images obtained from axial sections using a 103 objective on the NiE. Then, a threshold was separately applied to EGFP and turboRFP images, followed by binarization. Subsequently, $EGFP^+$ pixels were subtracted from the corresponding binarized turboRFP image, and $turboRFP^+$ pixels above threshold were quantified as the total area of $turboRFP^+$:$EGFP^-$ axon collaterals. This area was then normalized to the $turboRFP^+$:$EGFP^-$ CST axon number at C1–C2 to calculate the relative density of $turboRFP^+$:$EGFP^-$ axon collaterals in the cervical gray matter.

We utilized multiple approaches to label CSN, and there is variability in the overall extent of CSN axon labeling. For example, the density of CSN_{medial} axon collaterals labeled by AAV in Figure S3C is higher than the density of labeled CSN_{medial} axon collaterals in Figures 2D, 2E, 4D–4E, or 6B. In Figures 2D, 2E and 4D–4E, BDA iontophoresis into caudomedial sensorimotor cortex was used to label CSN_{medial} and trace their axons. BDA iontophoresis labels only cells that are closely adjacent to the tip of capillary filled with BDA, enabling focal labeling of cells. We see 309 ± 38 BDA-labeled CST axons at C1-C2 (mean ± SEM, n = 12; unilateral labeling). In Figure 6B, genetically encoded tdTomato protein expressed from the *ROSA26* locus upon activation of *Crim1*-CreER was used to label CSN_{TL}. Expression of tdTomato from both *ROSA26* loci initiated by tamoxifen injection at P3 labels 820 ± 97 CST axons at C1-C2 around 5-week old (mean ± SEM, n = 14; bilateral labeling). In Figure S3F, tdTomato-encoding AAV was injected into caudomedial sensorimotor cortex to label CSN_{medial}. AAV injections spread much wider than BDA. Further, we injected AAV-tdTomato at P4 when the mouse brain is substantially growing (as opposed to BDA iontophoretic injections or adult AAV injections which were performed in 4-week old mice). Therefore, 1,543 ± 269 CST axons were labeled via AAV in experiments described in Figure S3C (mean ± SEM, n = 6; unilateral labeling). We think that different tracing strategies for the most part explain the differences across experiments in the overall extent of labeled axon collateral density. Given the precision and targeted labeling of BDA, we used BDA iontophoresis in early experiments (described in Figures 2 and 4) to specifically label a small population of CSN_{medial}, and to convincingly illustrate axon collateral phenotypes in *Lumican* null mice. After these experiments, we transitioned to AAV and genetic labeling strategies to more efficiently conduct experiments as well as to utilize intersectional approaches, to address these questions further.

Behavioral tests—Mice that were tested on multiple behavioral paradigms were given a minimum 1-week resting period between tests. On days of training and testing, mice were moved to a test room 1 hour prior to training or testing for acclimation. Behavioral tests were performed during the light cycle. The investigator was blinded to the genotype of the mice throughout the training/testing and video analysis.

Open field test—For 3 days prior to testing, mice were habituated to a transport box and an open field arena (40 cm × 40 cm × 30 cm). Mice were then individually placed in the open field arena, and their activity was measured over a 10-min period with EthoVision XT (Noldus, VA). Within the assigned field and regions of interest, the software assessed basic locomotion parameters of the mice, including the total time moving and total distance moved. Adult female mice were tested when ~7–20 weeks old.

Balance beam test—The balance beam test was carried out using modifications of a previously reported method.[64] Mice traverse the length of a 12.7 or 9.5 mm wide, 30 cm long beam that is placed 26 cm above ground, with 10 min rest period between each run. On the day prior to testing, mice traverse the wider beam three times to habituate to the platform. On the following testing day, mice were digitally videotaped at 60 frames/sec from the left side while traversing the beam, and a mirror was placed on the right side to obtain both longitudinal views to accurately identify foot slips. Performance on each beam was quantified by measuring the time required for the mouse to traverse the beam between designated start/end points and the number of foot slips that occurred in the process. The number of forelimb and hindlimb foot slips in 3 runs for each beam width was measured and averaged. Adult female mice were tested when ~12–20 weeks old.

Food pellet grasping test—The basic training paradigm and chamber design were based on established methods.[61,62] The training chamber, slightly modified from previous versions (Chen et al., *J. Vis Exp*, 2014), was built from clear (front) and black (rear and both sides) Plexiglas (dimensions 20 cm high ×9 cm wide × 14 cm long). The bottom of the chamber is 5.5 cm tall and has 0.5 cm slits at 2 cm intervals, so that mice do not consume dropped food pellets. One vertical slit (0.5 cm wide; 10 cm high) is located in the center of the chamber's front wall. An exterior food tray is affixed to the wall in front of the slit 1.2 cm above the bottom of the chamber to hold a food pellet (dustless precision pellet, 20 mg, Bio-Serv). Food pellets were placed in an indentation 1 cm away from the front wall and 0.5 cm away from the center of the slit. Adult female mice were introduced to the test when ~12–18 weeks old.

We employed a standard paradigm of 6-day pre-training/shaping habituation and food restriction, followed by 10-day evaluation/training period (Figure 7B). After 1 day of group habituation to the chamber and group exposure to food pellets, mice were food-restricted throughout the shaping and training period to maintain ~90% of their original body weight. During the shaping period, mice were habituated individually to the chamber for 5 min over 2 days without food pellets, and for 8 min and 10 min over another 2 days with food pellets within tongue distance on the tray. Mice that did not show any interest in the food pellets at this time were excluded from subsequent training and analysis. Over the following 2 days, individual food pellets were placed on the tray outside the slit to practice pellet

grasping for 10 min. Gradually, pellets were placed further away on the tray and eventually in the indentation to force mice to reach for the pellet and to measure paw preference for subsequent training. No more than 5 reaches at the indentation distance were practiced to prevent over practice. During the subsequent 10-day training period, mice were trained every day in the reaching box for 10 min to conduct pellet grasping reaches. Only when the mouse successfully retrieved the food pellet and put it into its mouth was the reach considered a success. The number of successful reaches was divided by the number of total reaches to calculate success rate (percentage). Failed reaches were classified as reaching, grasping, or retrieving failures[60] with criteria established *a priori*. Mice were digitally videotaped at 60 frames/sec to monitor forelimb movement from front and both sides. Digital videos from multiple angles were analyzed to precisely assess each reach. Mice that showed no intention to retrieve food pellets or that consistently used their tongue instead of their forelimb to retrieve food pellets were excluded from further analysis. The standard duration of evaluative testing, or "training", period is 7–10 days,[15,60,62] and we performed the training for 10 days for maximal insight. We allowed the mice continued access to the apparatus and food pellets through training day 14 in anticipation of future reintroduction for a memory test,[62] in which we asked whether or not reduced pellet grasping success rate is due to a broader cognitive or memory defect. After the 10-day training period and 4-day access to the equipment, mice were fed *ad libitum*. Eighteen to 32 days after 10-day training period ended, mice were again food-restricted for 2 days, after which a single 10-min training ("memory test") was performed on the following day. As noted above, if there was a broader cognitive or memory defect in *Lumican* null mice, there would be a dramatic drop off in performance during this memory test. Indeed, no drop off in performance was observed in either wild-type or *Lumican* null mice; both show comparable success rate maintenance (1.4 ± 4.6% *vs.* 5.4 ± 3.3% increase, respectively; $p > 0.05$, two-tailed unpaired student's t-test) compared to the last day of the 10-day training period. These memory test results strongly reinforce that the evaluative testing/training appropriately measures forelimb grasping, and not theoretical memory disability.

QUANTIFICATION AND STATISTICAL ANALYSIS

The details of imaging quantification methodologies have been described in Method details. All n values, as well as p values obtained, are also listed in the figures and figure legends. GraphPad Prism or Microsoft Excel were used to perform statistical tests in this study. Data distributions were assumed to be normal, but this was not formally tested. We used two-tailed paired Student's t-test (Figure S1K), two-way repeated measures ANOVA (Figures 7B and S7A), or two-tailed unpaired Student's t-test (other statistical analyses). A p value of <0.05 was considered statistically significant. No statistical methods were used to pre-determine sample sizes.

Supplementary Material

Refer to Web version on PubMed Central for supplementary material.

ACKNOWLEDGMENTS

We thank T. Addison, K. Wang, M. Wettstein, and K. Yee for technical assistance; members of the Macklis laboratory for discussions and suggestions; the Harvard Center for Biological Imaging for infrastructure and support; the Harvard Center for Mass Spectrometry for LC-MS/MS analysis; D. Tillman for the assistance on proteomics data analysis; A.K. Engmann, K.J. Laboy-Juarez, and A.C. Mosberger for input on the pellet grasping test; A. Poulopoulos for discussions and reagents; and M. Hibi, S. Chakravarti, D. Comoletti, E. Kim, A. Ghosh, J. de Wit, G. Miyoshi, and Y. Mukouyama for generous sharing of mice and reagents. This work was supported by grants from the National Institutes of Health (R01s NS045523 and NS075672, with additional infrastructure supported by NS049553, NS104055, and DP1 NS106665), the ALS Association, the Travis Roy Foundation, and the Massachusetts Department of Public Health Spinal Cord Injury Fund to J.D.M. Y.I. was partially supported by the Uehara Memorial Foundation, the Kanae Foundation for the Promotion of Medical Science, the Murata Overseas Scholarship Foundation, and the DEARS Foundation. V.S. was partially supported by a National Institutes of Health K12 fellowship (NTRAIN/NICHD K12HD093427) and the DEARS Foundation. S.J.S. was partially supported by National Institutes of Health predoctoral National Research Service Award F31 NS063516. J.D.M. is an Allen Distinguished Investigator of the Paul G. Allen Frontiers Group.

INCLUSION AND DIVERSITY

We support inclusive, diverse, and equitable conduct of research.

REFERENCES

1. Kalil K, and Dent EW (2014). Branch management: mechanisms of axon branching in the developing vertebrate CNS. Nat. Rev. Neurosci. 15, 7–18. 10.1038/nrn3650. [PubMed: 24356070]
2. Chédotal A (2019). Roles of axon guidance molecules in neuronal wiring in the developing spinal cord. Nat. Rev. Neurosci. 20, 380–396. 10.1038/s41583-019-0168-7. [PubMed: 31000796]
3. Martini FJ, Guillamón-Vivancos T, Moreno-Juan V, Valdeolmillos M, and López-Bendito G (2021). Spontaneous activity in developing thalamic and cortical sensory networks. Neuron 109, 2519–2534. 10.1016/j.neuron.2021.06.026. [PubMed: 34293296]
4. Sahni V, Engmann A, Ozkan A, and Macklis JD (2020). Motor Cortex Connections, 2nd Edition (Elsevier).
5. Levine AJ, Lewallen KA, and Pfaff SL (2012). Spatial organization of cortical and spinal neurons controlling motor behavior. Curr. Opin. Neurobiol. 22, 812–821. 10.1016/j.conb.2012.07.002. [PubMed: 22841417]
6. Lemon RN (2008). Descending pathways in motor control. Annu. Rev. Neurosci. 31, 195–218. 10.1146/annurev.neuro.31.060407.125547. [PubMed: 18558853]
7. Martin JH (2005). The corticospinal system: from development to motor control. Neuroscientist 11, 161–173. 10.1177/1073858404270843. [PubMed: 15746384]
8. Dum RP, and Strick PL (2002). Motor areas in the frontal lobe of the primate. Physiol. Behav. 77, 677–682. 10.1016/s0031-9384(02)00929-0. [PubMed: 12527018]
9. Schieber MH (2007). Chapter 2 Comparative anatomy and physiology of the corticospinal system. Handb. Clin. Neurol. 82, 15–37. 10.1016/S0072-9752(07)80005-4. [PubMed: 18808887]
10. Penfield W, and Rasmussen T (1950). The Cerebral Cortex of Man; a Clinical Study of Localization of Function (Macmillan).
11. Woolsey CN, Settlage PH, Meyer DR, Sencer W, Pinto Hamuy T, and Travis AM (1952). Patterns of localization in precentral and “supplementary” motor areas and their relation to the concept of a premotor area. Res. Publ. Assoc. Res. Nerv. Ment. Dis. 30, 238–264. [PubMed: 12983675]
12. Donoghue JP, and Wise SP (1982). The motor cortex of the rat: cytoarchitecture and microstimulation mapping. J. Comp. Neurol. 212, 76–88. 10.1002/cne.902120106. [PubMed: 6294151]
13. Neafsey EJ, Bold EL, Haas G, Hurley-Gius KM, Quirk G, Sievert CF, and Terreberry RR (1986). The organization of the rat motor cortex: a microstimulation mapping study. Brain Res. 396, 77–96. [PubMed: 3708387]
14. Tennant KA, Adkins DL, Donlan NA, Asay AL, Thomas N, Kleim JA, and Jones TA (2011). The organization of the forelimb representation of the C57BL/6 mouse motor cortex as defined by

intracortical microstimulation and cytoarchitecture. Cerebr. Cortex 21, 865–876. 10.1093/cercor/bhq159.

15. Wang X, Liu Y, Li X, Zhang Z, Yang H, Zhang Y, Williams PR, Alwahab NSA, Kapur K, Yu B, et al. (2017). Deconstruction of corticospinal circuits for goal-directed motor skills. Cell 171, 440–455.e14. 10.1016/j.cell.2017.08.014. [PubMed: 28942925]
16. Liu Y, Latremoliere A, Li X, Zhang Z, Chen M, Wang X, Fang C, Zhu J, Alexandre C, Gao Z, et al. (2018). Touch and tactile neuropathic pain sensitivity are set by corticospinal projections. Nature 561, 547–550. 10.1038/s41586-018-0515-2. [PubMed: 30209395]
17. Ueno M, Nakamura Y, Li J, Gu Z, Niehaus J, Maezawa M, Crone SA, Goulding M, Baccei ML, and Yoshida Y (2018). Corticospinal circuits from the sensory and motor cortices differentially regulate skilled movements through distinct spinal interneurons. Cell Rep. 23, 1286–1300.e7. 10.1016/j.celrep.2018.03.137. [PubMed: 29719245]
18. Steward O, Yee KM, Metcalfe M, Willenberg R, Luo J, Azevedo R, Martin-Thompson JH, and Gandhi SP (2021). Rostro-caudal specificity of corticospinal tract projections in mice. Cerebr. Cortex 31, 2322–2344. 10.1093/cercor/bhaa338.
19. Kaas JH (2004). Evolution of somatosensory and motor cortex in primates. Anat. Rec. A Discov. Mol. Cell. Evol. Biol. 281, 1148–1156. 10.1002/ar.a.20120. [PubMed: 15470673]
20. Kaas JH (2013). The evolution of brains from early mammals to humans. Wiley Interdiscip. Rev. Cogn. Sci. 4, 33–45. 10.1002/wcs.1206. [PubMed: 23529256]
21. Krubitzer L (2007). The magnificent compromise: cortical field evolution in mammals. Neuron 56, 201–208. 10.1016/j.neuron.2007.10.002. [PubMed: 17964240]
22. Sahni V, Shnider SJ, Jabaudon D, Song JHT, Itoh Y, Greig LC, and Macklis JD (2021). Corticospinal neuron subpopulation-specific developmental genes prospectively indicate mature segmentally specific axon projection targeting. Cell Rep. 37, 109843. 10.1016/j.celrep.2021.109843. [PubMed: 34686320]
23. Sahni V, Itoh Y, Shnider SJ, and Macklis JD (2021). Crim1 and Kelch-like 14 exert complementary dual-directional developmental control over segmentally specific corticospinal axon projection targeting. Cell Rep. 37, 109842. 10.1016/j.celrep.2021.109842. [PubMed: 34686337]
24. Greig LC, Woodworth MB, Galazo MJ, Padmanabhan H, and Macklis JD (2013). Molecular logic of neocortical projection neuron specification, development and diversity. Nat. Rev. Neurosci. 14, 755–769. 10.1038/nrn3586. [PubMed: 24105342]
25. Ozkan A, MacDonald JL, Fame RM, Itoh Y, Peter M, Durak O, and Macklis JD (2020). Specification of Cortical Projection Neurons: Transcriptional Mechanisms, 2nd Edition (Elsevier).
26. Ueno M, Fujita Y, Tanaka T, Nakamura Y, Kikuta J, Ishii M, and Yamashita T (2013). Layer V cortical neurons require microglial support for survival during postnatal development. Nat. Neurosci. 16, 543–551. 10.1038/nn.3358. [PubMed: 23525041]
27. Thion MS, Ginhoux F, and Garel S (2018). Microglia and early brain development: an intimate journey. Science 362, 185–189. 10.1126/science.aat0474. [PubMed: 30309946]
28. Canty AJ, and Murphy M (2008). Molecular mechanisms of axon guidance in the developing corticospinal tract. Prog. Neurobiol. 85, 214–235. 10.1016/j.pneurobio.2008.02.001. [PubMed: 18378059]
29. Lilley BN, Pan YA, and Sanes JR (2013). SAD kinases sculpt axonal arbors of sensory neurons through long- and short-term responses to neurotrophin signals. Neuron 79, 39–53. 10.1016/j.neuron.2013.05.017. [PubMed: 23790753]
30. Brézillon S, Pietraszek K, Maquart FX, and Wegrowski Y (2013). Lumican effects in the control of tumour progression and their links with metalloproteinases and integrins. FEBS J. 280, 2369–2381. 10.1111/febs.12210. [PubMed: 23438179]
31. Chen S, and Birk DE (2013). The regulatory roles of small leucine-rich proteoglycans in extracellular matrix assembly. FEBS J. 280, 2120–2137. 10.1111/febs.12136. [PubMed: 23331954]
32. Caterson B, and Melrose J (2018). Keratan sulfate, a complex glycosaminoglycan with unique functional capability. Glycobiology 28, 182–206. 10.1093/glycob/cwy003. [PubMed: 29340594]
33. Tessier-Lavigne M, and Goodman CS (1996). The molecular biology of axon guidance. Science 274, 1123–1133. 10.1126/science.274.5290.1123. [PubMed: 8895455]

34. Lowery LA, and Van Vactor D (2009). The trip of the tip: understanding the growth cone machinery. Nat. Rev. Mol. Cell Biol. 10, 332–343. 10.1038/nrm2679. [PubMed: 19373241]
35. Long KR, Newland B, Florio M, Kalebic N, Langen B, Kolterer A, Wimberger P, and Huttner WB (2018). Extracellular matrix components HAPLN1, lumican, and collagen I cause hyaluronic acid-dependent folding of the developing human neocortex. Neuron 99, 702–719.e6. 10.1016/j.neuron.2018.07.013. [PubMed: 30078576]
36. Arlotta P, Molyneaux BJ, Chen J, Inoue J, Kominami R, and Macklis JD (2005). Neuronal subtype-specific genes that control corticospinal motor neuron development in vivo. Neuron 45, 207–221. 10.1016/j.neuron.2004.12.036. [PubMed: 15664173]
37. Alcamo EA, Chirivella L, Dautzenberg M, Dobreva G, Fariñas I, Grosschedl R, and McConnell SK (2008). Satb2 regulates callosal projection neuron identity in the developing cerebral cortex. Neuron 57, 364–377. 10.1016/j.neuron.2007.12.012. [PubMed: 18255030]
38. Britanova O, de Juan Romero C, Cheung A, Kwan KY, Schwark M, Gyorgy A, Vogel T, Akopov S, Mitkovski M, Agoston D, et al. (2008). Satb2 is a postmitotic determinant for upper-layer neuron specification in the neocortex. Neuron 57, 378–392. 10.1016/j.neuron.2007.12.028. [PubMed: 18255031]
39. Leone DP, Heavner WE, Ferenczi EA, Dobreva G, Huguenard JR, Grosschedl R, and McConnell SK (2015). Satb2 regulates the differentiation of both callosal and subcerebral projection neurons in the developing cerebral cortex. Cerebr. Cortex 25, 3406–3419. 10.1093/cercor/bhu156.
40. Chen B, Schaevitz LR, and McConnell SK (2005). Fezl regulates the differentiation and axon targeting of layer 5 subcortical projection neurons in cerebral cortex. Proc. Natl. Acad. Sci. USA 102, 17184–17189. [PubMed: 16284245]
41. Molyneaux BJ, Arlotta P, Hirata T, Hibi M, and Macklis JD (2005). Fezl is required for the birth and specification of corticospinal motor neurons. Neuron 47, 817–831. 10.1016/j.neuron.2005.08.030. [PubMed: 16157277]
42. Silver J, and Miller JH (2004). Regeneration beyond the glial scar. Nat. Rev. Neurosci. 5, 146–156. 10.1038/nrn1326nrn1326. [PubMed: 14735117]
43. Snow DM, Steindler DA, and Silver J (1990). Molecular and cellular characterization of the glial roof plate of the spinal cord and optic tectum: a possible role for a proteoglycan in the development of an axon barrier. Dev. Biol. 138, 359–376. 10.1016/0012-1606(90)90203-u. [PubMed: 1690673]
44. Jones LL, and Tuszynski MH (2002). Spinal cord injury elicits expression of keratan sulfate proteoglycans by macrophages, reactive microglia, and oligodendrocyte progenitors. J. Neurosci. 22, 4611–4624. [PubMed: 12040068]
45. Ito Z, Sakamoto K, Imagama S, Matsuyama Y, Zhang H, Hirano K, Ando K, Yamashita T, Ishiguro N, and Kadomatsu K (2010). N-acetylglucosamine 6-O-sulfotransferase-1-deficient mice show better functional recovery after spinal cord injury. J. Neurosci. 30, 5937–5947. 10.1523/JNEUROSCI.2570-09.2010. [PubMed: 20427653]
46. Grover J, Chen XN, Korenberg JR, and Roughley PJ (1995). The human lumican gene. Organization, chromosomal location, and expression in articular cartilage. J. Biol. Chem. 270, 21942–21949. 10.1074/jbc.270.37.21942. [PubMed: 7665616]
47. Chakravarti S, Magnuson T, Lass JH, Jepsen KJ, LaMantia C, and Carroll H (1998). Lumican regulates collagen fibril assembly: skin fragility and corneal opacity in the absence of lumican. J. Cell Biol. 141, 1277–1286. [PubMed: 9606218]
48. Bareyre FM, Kerschensteiner M, Misgeld T, and Sanes JR (2005). Transgenic labeling of the corticospinal tract for monitoring axonal responses to spinal cord injury. Nat. Med. 11, 1355–1360. 10.1038/nm1331. [PubMed: 16286922]
49. Kamiyama T, Kameda H, Murabe N, Fukuda S, Yoshioka N, Mizukami H, Ozawa K, and Sakurai M (2015). Corticospinal tract development and spinal cord innervation differ between cervical and lumbar targets. J. Neurosci. 35, 1181–1191. 10.1523/JNEUROSCI.2842-13.2015. [PubMed: 25609632]
50. Kuang RZ, and Kalil K (1994). Development of specificity in corticospinal connections by axon collaterals branching selectively into appropriate spinal targets. J. Comp. Neurol. 344, 270–282. 10.1002/cne.903440208. [PubMed: 8077461]

51. Kim S, Burette A, Chung HS, Kwon SK, Woo J, Lee HW, Kim K, Kim H, Weinberg RJ, and Kim E (2006). NGL family PSD-95-interacting adhesion molecules regulate excitatory synapse formation. Nat. Neurosci. 9, 1294–1301. 10.1038/nn1763. [PubMed: 16980967]
52. O'Sullivan ML, de Wit J, Savas JN, Comoletti D, Otto-Hitt S, Yates JR, and Ghosh A (2012). FLRT proteins are endogenous latrophilin ligands and regulate excitatory synapse development. Neuron 73, 903–910. 10.1016/j.neuron.2012.01.018. [PubMed: 22405201]
53. de Wit J, and Ghosh A (2016). Specification of synaptic connectivity by cell surface interactions. Nat. Rev. Neurosci. 17, 22–35. 10.1038/nrn.2015.3. [PubMed: 26656254]
54. Seiradake E, del Toro D, Nagel D, Cop F, Härtl R, Ruff T, Seyit-Bremer G, Harlos K, Border EC, Acker-Palmer A, et al. (2014). FLRT structure: balancing repulsion and cell adhesion in cortical and vascular development. Neuron 84, 370–385. 10.1016/j.neuron.2014.10.008. [PubMed: 25374360]
55. Feiner L, Koppel AM, Kobayashi H, and Raper JA (1997). Secreted chick semaphorins bind recombinant neuropilin with similar affinities but bind different subsets of neurons in situ. Neuron 19, 539–545. 10.1016/s0896-6273(00)80370-0. [PubMed: 9331347]
56. Lein ES, Hawrylycz MJ, Ao N, Ayres M, Bensinger A, Bernard A, Boe AF, Boguski MS, Brockway KS, Byrnes EJ, et al. (2007). Genome-wide atlas of gene expression in the adult mouse brain. Nature 445, 168–176. 10.1038/nature05453. [PubMed: 17151600]
57. Hanayama R, Tanaka M, Miwa K, Shinohara A, Iwamatsu A, and Nagata S (2002). Identification of a factor that links apoptotic cells to phagocytes. Nature 417, 182–187. 10.1038/417182a. [PubMed: 12000961]
58. Li Q, and Martin JH (2002). Postnatal development of connectional specificity of corticospinal terminals in the cat. J. Comp. Neurol. 447, 57–71. 10.1002/cne.10203. [PubMed: 11967895]
59. Clancy B, Darlington RB, and Finlay BL (2001). Translating developmental time across mammalian species. Neuroscience 105, 7–17. 10.1016/s0306-4522(01)00171-3. [PubMed: 11483296]
60. Gu Z, Serradj N, Ueno M, Liang M, Li J, Baccei ML, Martin JH, and Yoshida Y (2017). Skilled movements require non-apoptotic bax/bak pathway-mediated corticospinal circuit reorganization. Neuron 94, 626–641.e4. 10.1016/j.neuron.2017.04.019. [PubMed: 28472660]
61. Whishaw IQ (1996). An endpoint, descriptive, and kinematic comparison of skilled reaching in mice (Mus musculus) with rats (Rattus norvegicus). Behav. Brain Res. 78, 101–111. 10.1016/0166-4328(95)00236-7. [PubMed: 8864042]
62. Chen CC, Gilmore A, and Zuo Y (2014). Study motor skill learning by single-pellet reaching tasks in mice. JoVE 4, 51238. 10.3791/51238.
63. Shimogori T, Abe A, Go Y, Hashikawa T, Kishi N, Kikuchi SS, Kita Y, Niimi K, Nishibe H, Okuno M, et al. (2018). Digital gene atlas of neonate common marmoset brain. Neurosci. Res. 128, 1–13. 10.1016/j.neures.2017.10.009. [PubMed: 29111135]
64. Luong TN, Carlisle HJ, Southwell A, and Patterson PH (2011). Assessment of motor balance and coordination in mice using the balance beam. JoVE. 10.3791/2376.
65. Ozdinler PH, and Macklis JD (2006). IGF-I specifically enhances axon outgrowth of corticospinal motor neurons. Nat. Neurosci. 9, 1371–1381. 10.1038/nn1789. [PubMed: 17057708]
66. Cederquist GY, Azim E, Shnider SJ, Padmanabhan H, and Macklis JD (2013). Lmo4 establishes rostral motor cortex projection neuron subtype diversity. J. Neurosci. 33, 6321–6332. 10.1523/JNEUROSCI.5140-12.2013. [PubMed: 23575831]
67. Bakola S, Burman KJ, and Rosa MGP (2015). The cortical motor system of the marmoset monkey (Callithrix jacchus). Neurosci. Res. 93, 72–81. 10.1016/j.neures.2014.11.003. [PubMed: 25498953]
68. Imai T, and Sakano H (2011). Axon-axon interactions in neuronal circuit assembly: lessons from olfactory map formation. Eur. J. Neurosci. 34, 1647–1654. 10.1111/j.1460-9568.2011.07817.x. [PubMed: 22103421]
69. Wang L, and Marquardt T (2013). What axons tell each other: axon-axon signaling in nerve and circuit assembly. Curr. Opin. Neurobiol. 23, 974–982. 10.1016/j.conb.2013.08.004. [PubMed: 23973157]

70. Daoud H, Valdmanis PN, Gros-Louis F, Belzil V, Spiegelman D, Henrion E, Diallo O, Desjarlais A, Gauthier J, Camu W, et al. (2011). Resequencing of 29 candidate genes in patients with familial and sporadic amyotrophic lateral sclerosis. Arch. Neurol. 68, 587–593. 10.1001/archneurol.2010.351. [PubMed: 21220648]
71. Ravits J, Appel S, Baloh RH, Barohn R, Brooks BR, Elman L, Floeter MK, Henderson C, Lomen-Hoerth C, Macklis JD, et al. (2013). Deciphering amyotrophic lateral sclerosis: what phenotype, neuropathology and genetics are telling us about pathogenesis. Amyotroph. Lateral Scler. Frontotemporal Degener. 14, 5–18. 10.3109/21678421.2013.778548. [PubMed: 23678876]
72. Taylor JP, Brown RH, and Cleveland DW (2016). Decoding ALS: from genes to mechanism. Nature 539, 197–206. 10.1038/nature20413. [PubMed: 27830784]
73. Bareyre FM, Haudenschild B, and Schwab ME (2002). Long-lasting sprouting and gene expression changes induced by the monoclonal antibody IN-1 in the adult spinal cord. J. Neurosci. 22, 7097–7110. [PubMed: 12177206]
74. Ghosh A, Haiss F, Sydekum E, Schneider R, Gullo M, Wyss MT, Mueggler T, Baltes C, Rudin M, Weber B, and Schwab ME (2010). Rewiring of hindlimb corticospinal neurons after spinal cord injury. Nat. Neurosci. 13, 97–104. 10.1038/nn.2448. [PubMed: 20010824]
75. Oudega M, and Perez MA (2012). Corticospinal reorganization after spinal cord injury. J. Physiol. 590, 3647–3663. 10.1113/jphysiol.2012.233189. [PubMed: 22586214]
76. Tsata V, Möllmert S, Schweitzer C, Kolb J, Möckel C, Böhm B, Rosso G, Lange C, Lesche M, Hammer J, et al. (2021). A switch in *pdgfrb*$^{+}$ cell-derived ECM composition prevents inhibitory scarring and promotes axon regeneration in the zebrafish spinal cord. Dev. Cell 56, 509–524.e9. 10.1016/j.devcel.2020.12.009. [PubMed: 33412105]
77. Kaiser J, Maibach M, Salpeter I, Hagenbuch N, de Souza VBC, Robinson MD, and Schwab ME (2019). The spinal transcriptome after cortical stroke: in search of molecular factors regulating spontaneous recovery in the spinal cord. J. Neurosci. 39, 4714–4726. 10.1523/JNEUROSCI.2571-18.2019. [PubMed: 30962276]
78. Economo MN, Viswanathan S, Tasic B, Bas E, Winnubst J, Menon V, Graybuck LT, Nguyen TN, Smith KA, Yao Z, et al. (2018). Distinct descending motor cortex pathways and their roles in movement. Nature 563, 79–84. 10.1038/s41586-018-0642-9. [PubMed: 30382200]
79. Tasic B, Yao Z, Graybuck LT, Smith KA, Nguyen TN, Bertagnolli D, Goldy J, Garren E, Economo MN, Viswanathan S, et al. (2018). Shared and distinct transcriptomic cell types across neocortical areas. Nature 563, 72–78. 10.1038/s41586-018-0654-5. [PubMed: 30382198]
80. Poulopoulos A, Murphy AJ, Ozkan A, Davis P, Hatch J, Kirchner R, and Macklis JD (2019). Subcellular transcriptomes and proteomes of developing axon projections in the cerebral cortex. Nature 565, 356–360. 10.1038/s41586-018-0847-y. [PubMed: 30626971]
81. Engmann AK, Hatch JJ, Nanda P, Veeraraghavan P, Ozkan A, Poulopoulos A, Murphy AJ, and Macklis JD (2022). Neuronal subtype-specific growth cone and soma purification from mammalian CNS via fractionation and fluorescent sorting for subcellular analyses and spatial mapping of local transcriptomes and proteomes. Nat. Protoc. 17, 222–251. 10.1038/s41596-021-00638-7. [PubMed: 35022617]
82. Kaiser J, Patel P, Dündar F, Perez-Tetuan J, Angira N, Sieger E, and Sahni V (2022). Molecular specification of cortico-brainstem versus corticospinal projection neurons in development. Preprint at bioRxiv. 10.1101/2022.05.31.494253.
83. Maguire CA, Bovenberg MS, Crommentuijn MH, Niers JM, Kerami M, Teng J, Sena-Esteves M, Badr CE, and Tannous BA (2013). Triple bioluminescence imaging for in vivo monitoring of cellular processes. Mol. Ther. Nucleic Acids 2, e99. 10.1038/mtna.2013.25. [PubMed: 23778500]
84. Madisen L, Garner AR, Shimaoka D, Chuong AS, Klapoetke NC, Li L, van der Bourg A, Niino Y, Egolf L, Monetti C, et al. (2015). Transgenic mice for intersectional targeting of neural sensors and effectors with high specificity and performance. Neuron 85, 942–958. 10.1016/j.neuron.2015.02.022. [PubMed: 25741722]
85. Oh SW, Harris JA, Ng L, Winslow B, Cain N, Mihalas S, Wang Q, Lau C, Kuan L, Henry AM, et al. (2014). A mesoscale connectome of the mouse brain. Nature 508, 207–214. 10.1038/nature13186. [PubMed: 24695228]

86. Hirata T, Suda Y, Nakao K, Narimatsu M, Hirano T, and Hibi M (2004). Zinc finger gene fez-like functions in the formation of subplate neurons and thalamocortical axons. Dev. Dynam. 230, 546–556. 10.1002/dvdy.20068.

87. Gorski JA, Talley T, Qiu M, Puelles L, Rubenstein JLR, and Jones KR (2002). Cortical excitatory neurons and glia, but not GABAergic neurons, are produced in the Emx1-expressing lineage. J. Neurosci. 22, 6309–6314. [PubMed: 12151506]

88. Wuttke TV, Markopoulos F, Padmanabhan H, Wheeler AP, Murthy VN, and Macklis JD (2018). Developmentally primed cortical neurons maintain fidelity of differentiation and establish appropriate functional connectivity after transplantation. Nat. Neurosci. 21, 517–529. 10.1038/s41593-018-0098-0. [PubMed: 29507412]

89. Tervo DGR, Hwang BY, Viswanathan S, Gaj T, Lavzin M, Ritola KD, Lindo S, Michael S, Kuleshova E, Ojala D, et al. (2016). A designer AAV variant permits efficient retrograde access to projection neurons. Neuron 92, 372–382. 10.1016/j.neuron.2016.09.021. [PubMed: 27720486]

90. Schindelin J, Arganda-Carreras I, Frise E, Kaynig V, Longair M, Pietzsch T, Preibisch S, Rueden C, Saalfeld S, Schmid B, et al. (2012). Fiji: an open-source platform for biological-image analysis. Nat. Methods 9, 676–682. 10.1038/nmeth.2019. [PubMed: 22743772]

91. Zhang X, Smits AH, van Tilburg GB, Ovaa H, Huber W, and Vermeulen M (2018). Proteome-wide identification of ubiquitin interactions using UbIA-MS. Nat. Protoc. 13, 530–550. 10.1038/nprot.2017.147. [PubMed: 29446774]

92. Grider MH, Chen Q, and Shine HD (2006). Semi-automated quantification of axonal densities in labeled CNS tissue. J. Neurosci. Methods 155, 172–179. 10.1016/j.jneumeth.2005.12.021. [PubMed: 16469388]

Highlights

- Evolutionarily newer, bulbar-cervical projecting rostrolateral CSN express Lumican
- Lumican suppresses axon collaterals formed by evolutionarily older medial CSN populations
- Lumican null mice exhibit reduced forelimb dexterity
- Lumican potentially enabled evolutionary diversification of corticospinal circuitry

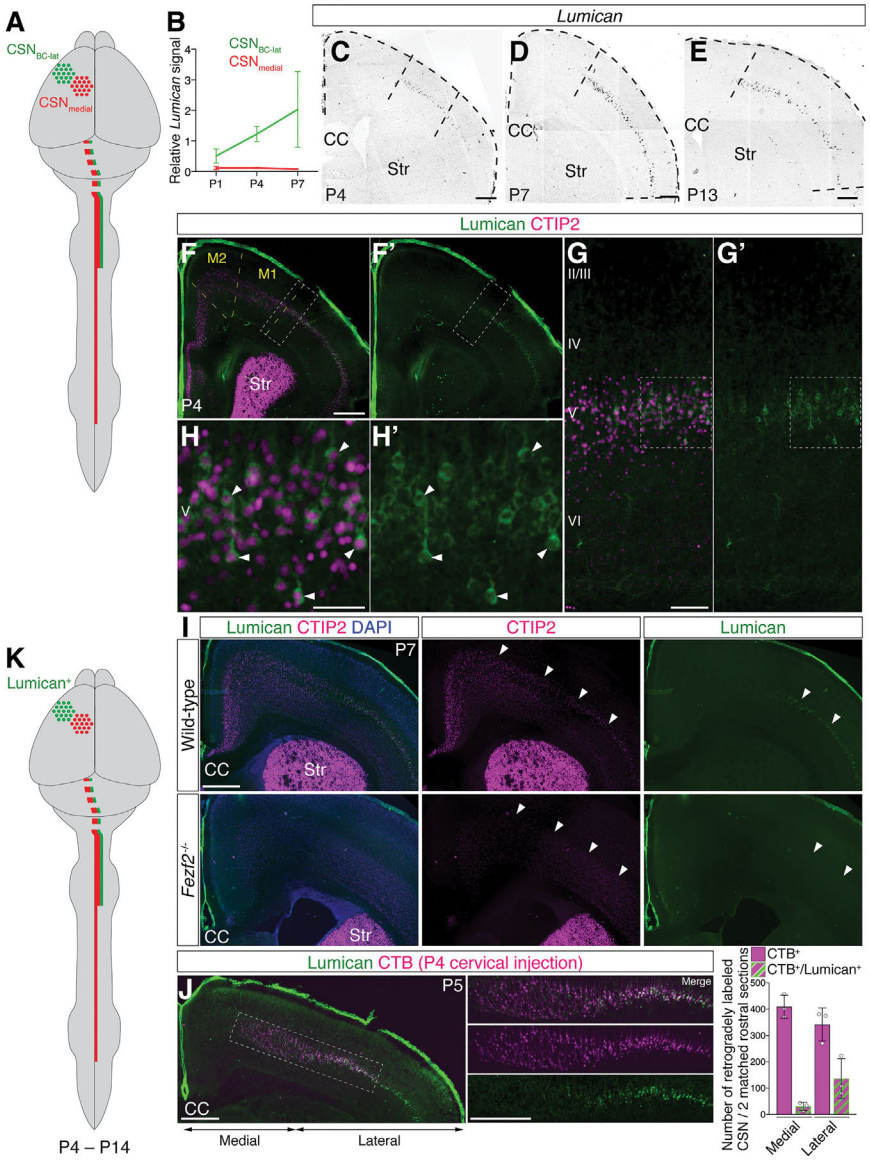

Figure 1. Lumican is expressed by $CSN_{BC\text{-}lat}$ in postnatal developing cortex in mice

(A) Schematized representation of developmentally distinct CSN subpopulations. CSN in rostrolateral sensorimotor cortex ($CSN_{BC\text{-}lat}$; green) and CSN in caudomedial sensorimotor cortex (CSN_{medial}; red) are illustrated. For simplicity, axon collaterals are not illustrated, and CSN are illustrated in only one hemisphere.

(B) Temporal profile of *Lumican* expression from microarray analysis. $CSN_{BC\text{-}lat}$, green; CSN_{medial}, red. The y axis represents normalized expression level; data are presented as the mean ± SD, n = 2–3.

(C–E) *In situ* hybridization on coronal brain sections reveals that *Lumican* is expressed exclusively in lateral cortex. Scale bars, 400 μm.

(F–H) Immunocytochemistry on coronal P4 brain section detects Lumican expression (green) only in lateral cortex, while it is not detected medially (F, F′). Lumican is expressed specifically in layer V (G, G′), and virtually all Lumican-positive cells co-express CTIP2

(magenta) (H, H′). Arrowheads indicate neurons co-expressing Lumican and CTIP2. Scale bars, 500 μm (F); 100 μm (G); 50 μm (H).

(I) There is no Lumican expression (green) in P7 *Fezf2* null cortex, while meningeal Lumican expression is preserved. Arrowheads indicate layer V neurons expressing CTIP2 and Lumican in wild-type cortex, which are absent in *Fezf2* null cortex. CTIP2, magenta; DAPI, blue. Scale bar, 500 μm.

(J) Lumican (green) immunocytochemistry on coronal section of P5 brain retrogradely labeled by CTB-555 (magenta) injection into the cervical dorsal funiculus at P4. Co-labeling by Lumican and CTB is observed predominantly in lateral cortex, demonstrating Lumican expression selectively by $CSN_{BC\text{-}lat}$. Mean ± SD, n = 3. Scale bars, 500 μm.

(K) Schematized representation of Lumican expression by developing $CSN_{BC\text{-}lat}$ (green) between P4 and P14.

CC, corpus callosum; M1, primary motor cortex; M2, secondary motor cortex; Str, striatum. See also Figure S1.

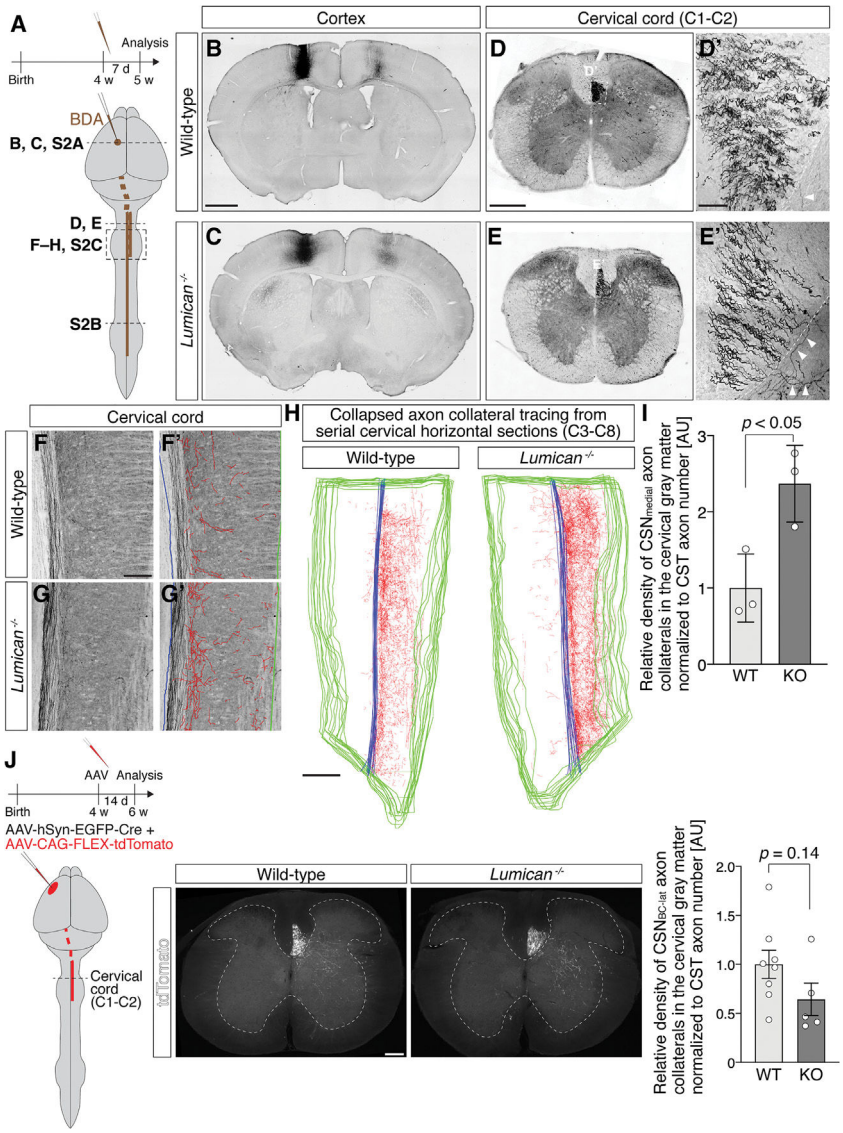

Figure 2. Lumican suppresses CSN_{medial} axon collateralization in the cervical cord in a non-cell-autonomous manner

(A) Schematic illustrating the experimental outline for (B–I).

(B and C) Representative coronal brain sections showing BDA injection site in M1. BDA, black. Scale bar, 1 mm.

(D and E) Axial sections of cervical cord (C1–C2 level) show corticospinal axons entering the spinal cord. CST axons in the dorsal funiculus are enlarged in magnified images (D′ and E′). Note exuberant axon collateralization (white arrowheads) in *Lumican* null cervical gray matter, quite rare in wild type. BDA, black. Scale bars, 500 μm (D, E); 50 μm (D′, E′).

(F and G) Horizontal sections of cervical cord show collateral innervation into the gray matter. Manually traced axon collaterals are labeled in red. Midline and outer border of gray matter are labeled in blue and green, respectively (F′, G′). BDA, black. Scale bar, 200 μm.

(H) Manually traced axon collaterals (red) on serial horizontal sections (C3–C8) are collapsed onto a single plane image, together with midline (blue) and gray matter border (green). Scale bar, 500 μm.

(I) Quantification of relative corticospinal axon collateral density in the cervical gray matter normalized to CST axon number at C1–C2 shows increased CSN_{medial} axon collateralization in *Lumican* null mice compared with wild-type mice. Mean ± SD, n = 3, Student's t test. WT, wild-type; KO, *Lumican* null.

(J) Schematic illustrates the experimental outline. AAVs encoding Cre recombinase (at a lower titer) and Cre-dependent tdTomato (at a higher titer) are stereotactically injected into rostrolateral sensorimotor cortex. Axial sections of C1–C2 cervical cord display tdTomato fluorescence in the dorsal funiculus and gray matter. Dashed lines demarcate gray matter. Quantification of relative density of $CSN_{BC\text{-}lat}$ axon collaterals normalized to CST axon number at C1–C2 does not show a significant change in *Lumican* null compared with wild-type mice, although there appears to be a trend toward a modest reduction in *Lumican* null mice (see discussion). Mean ± SEM, n = 8 (wild type) or 5 (*Lumican* null), Student's t test. Scale bar, 200 μm.

See also Figure S2.

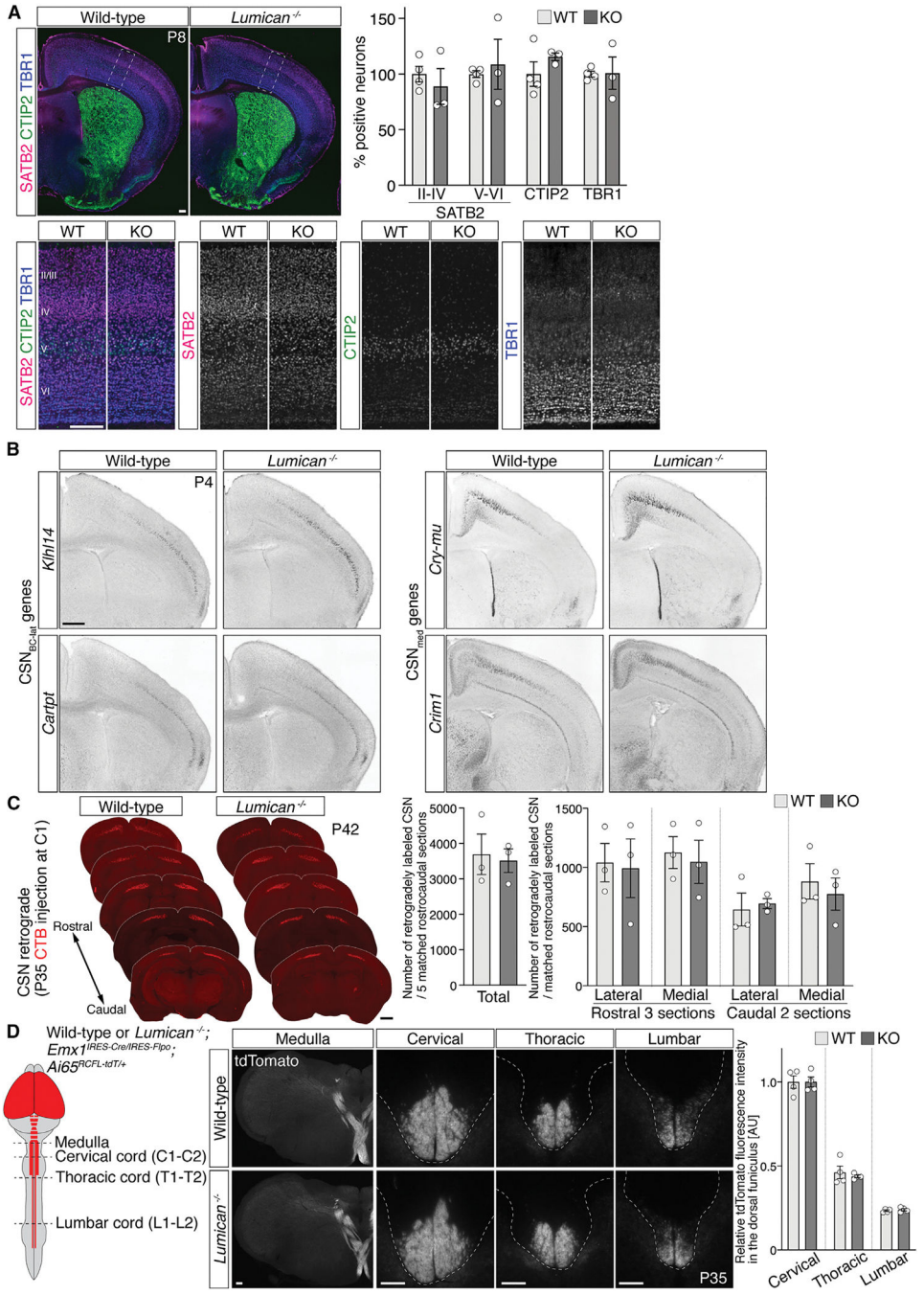

Figure 3. CSN specification and axon extension are unchanged in *Lumican* null mice

(A) In the absence of *Lumican*, overall brain structure remains unchanged. SCPN, CPN, and CThPN marker and control molecules CTIP2, SATB2, and TBR1, respectively, are expressed and positioned normally at P8. Quantification of the number of neurons expressing these molecules in *Lumican* null primary somatosensory cortex is presented as a percentage of wild-type neurons. Mean ± SEM, n = 4 (wild type) or 3 (*Lumican* null). Scale bars, 200 μm.

(B) Expression of $CSN_{BC\text{-}lat}$-specific genes *Klhl14* and *Cartpt* and CSN_{medial}-specific genes *Cry-mu* and *Crim1* is essentially indistinguishable between wild-type and *Lumican* null cortex at P4. Scale bar, 200 μm.

(C) Total number and distribution of retrogradely labeled CSN are indistinguishable between wild-type and *Lumican* null cortex. Mean ± SEM, n = 3. Scale bar, 1 mm.

(D) CST axons are anterogradely labeled by $Emx1^{IRES\text{-}Cre/IRES\text{-}Flpo}$;$Ai65^{RCFL\text{-}tdT/+}$. *Lumican* null CST axons normally decussate in the medulla and extend in the spinal cord. Mean ± SEM, n = 4. Scale bars, 100 μm.

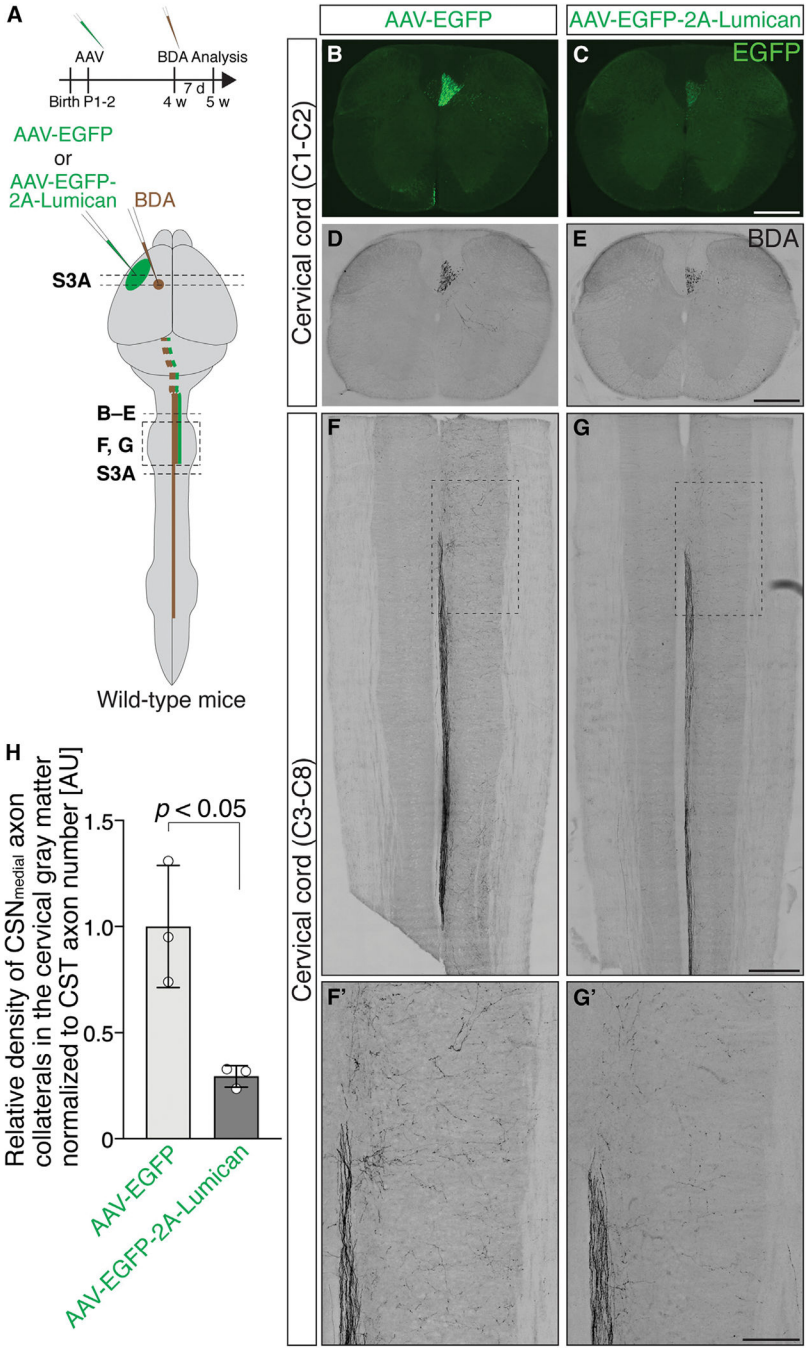

Figure 4. Lumican overexpression by $CSN_{BC\text{-}lat}$ non-cell-autonomously suppresses CSN_{medial} axon collateralization in the cervical cord

(A) Schematic illustrating the experimental outline. (B–E) Axial sections of C1–C2 cervical cord show corticospinal axons labeled by AAV-derived EGFP (green; B and C) or BDA (black; D and E). Scale bars, 500 m.

(F and G) Horizontal sections of cervical cord (C3– C8) display CSN_{medial} axon collateral innervation into the gray matter. BDA, black. Scale bars, 500 μm (F, G); 200 μm (F′, G′).

(H) Quantification of relative corticospinal axon collateral density normalized to CST axon number at C1–C2 shows that Lumican overexpression by $CSN_{BC\text{-}lat}$ substantially reduces CSN_{medial} axon collateralization. Mean ± SD, n = 3, Student's t test.
See also Figures S3 and S4.

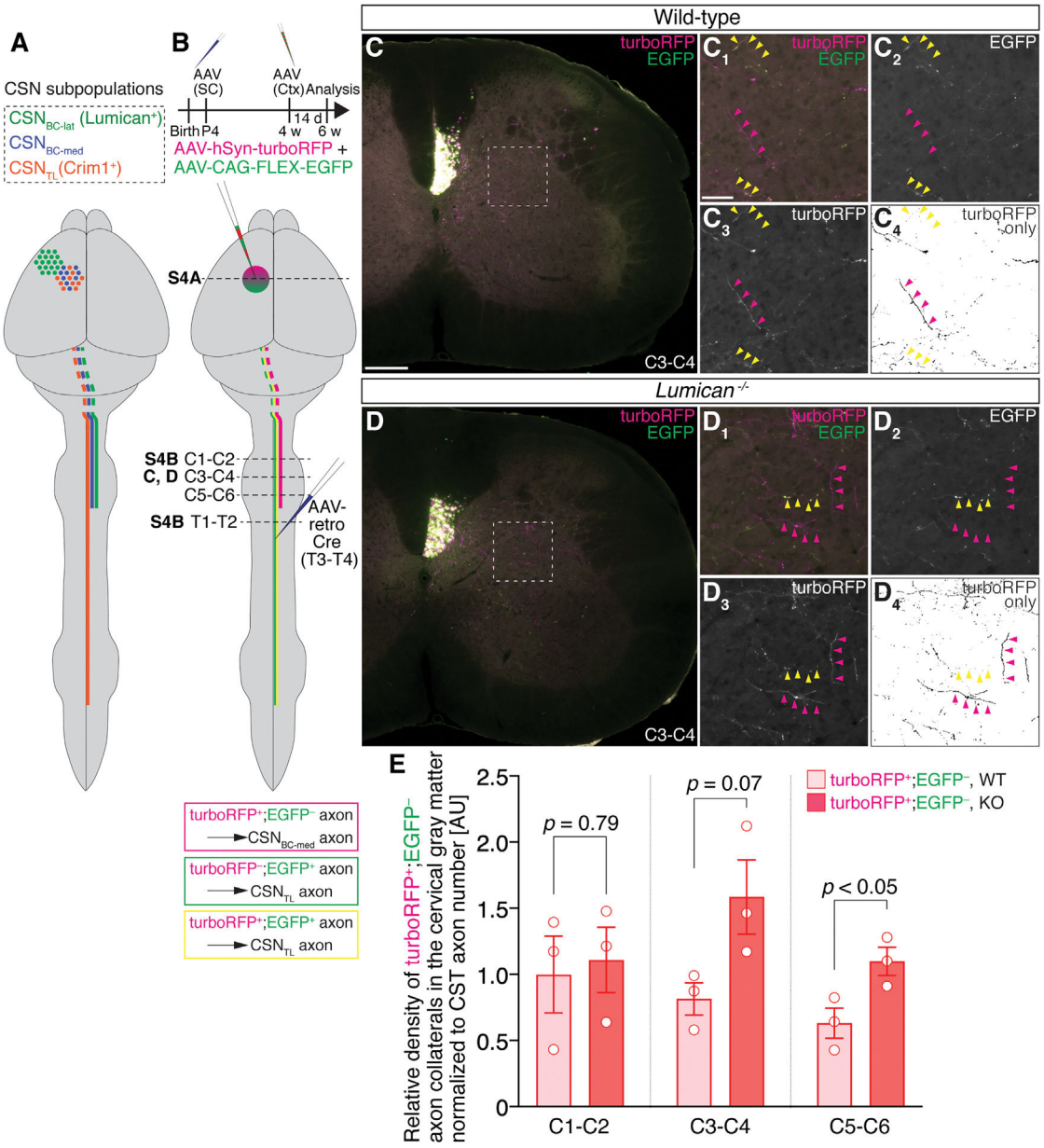

Figure 5. Exclusionary, subtractive viral labeling reveals increased $CSN_{BC\text{-}med}$ axon collateralization in *Lumican* null cervical cord

(A) Schematized representation of developmentally distinct CSN subpopulations by the combination of location and projection specificity. Compared with the schematic in Figure 1A, CSN in caudomedial sensorimotor cortex (CSN_{medial}) are further subdivided into $CSN_{BC\text{-}med}$ (blue) and CSN_{TL} (orange). While $CSN_{BC\text{-}med}$ send projections only to brainstem and cervical cord, CSN_{TL} axons extend and collateralize throughout the spinal cord. For simplicity, axon collaterals are not illustrated, and CSN are illustrated in only one hemisphere.

(B) Schematic illustrating the experimental outline.

(C and D) Axial sections of C3–C4 cervical cord show turboRFP and EGFP fluorescence in the dorsal funiculus and gray matter. In higher-magnification images ($C_{1–4}$, $D_{1–4}$),

magenta arrowheads indicate turboRFP^{+};EGFP^{-} axon collaterals, while yellow arrowheads indicate turboRFP^{+};EGFP^{+} axon collaterals. To identify turboRFP^{+};EGFP^{-} collateral signal, turboRFP^{+} and EGFP^{+} pixels above threshold are separately identified, followed by subtraction of EGFP^{+} pixels from turboRFP channel (C_4, D_4). Scale bars, 200 μm (C, D); 50 μm ($C_{1–4}$, $D_{1–4}$).

(E) Quantification of relative density of turboRFP^{+};EGFP^{-} axon collateral density normalized to CST axon number at C1–C2. Mean ± SEM, n = 3, Student's t test.

See also Figure S5.

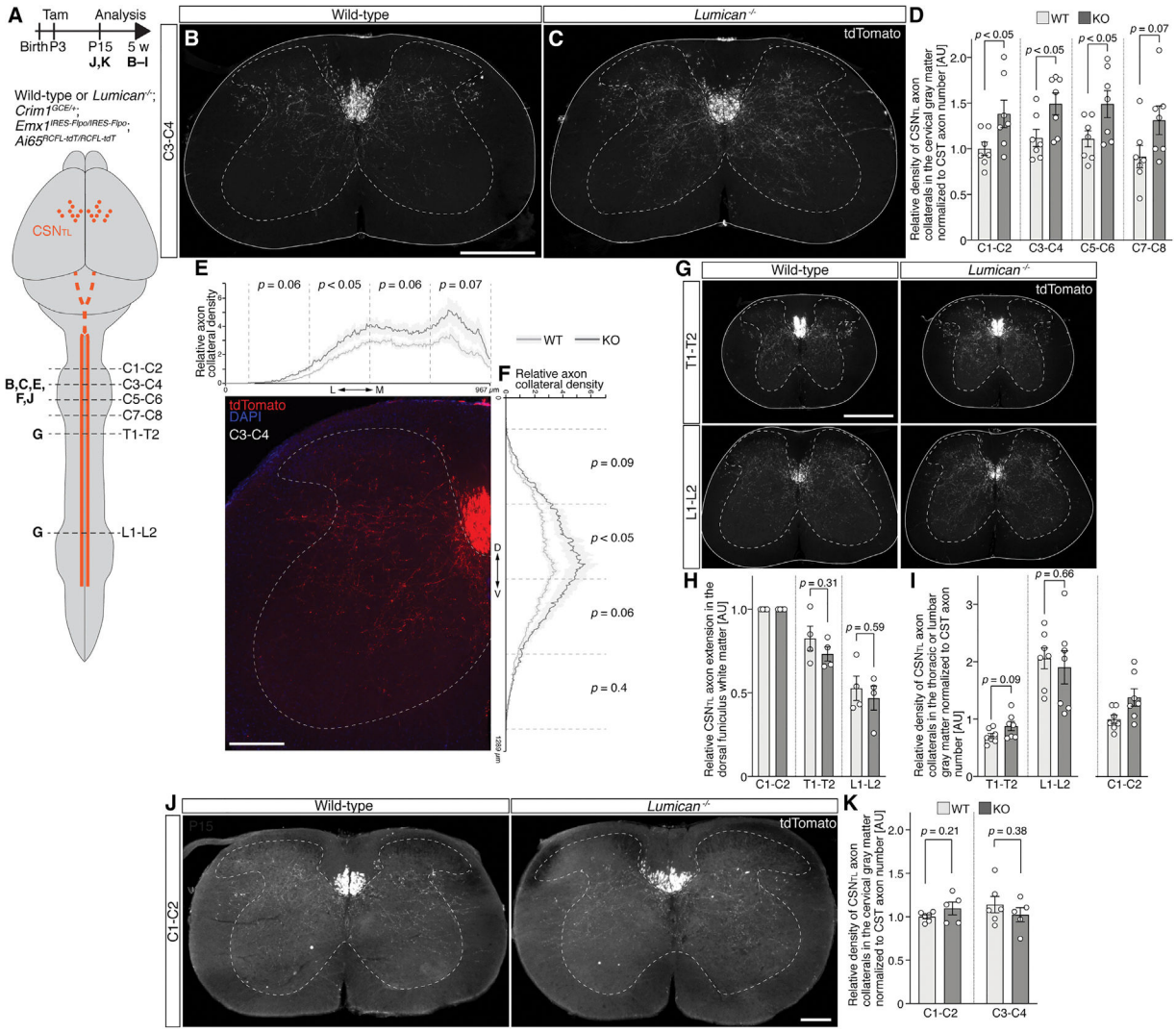

Figure 6. Intersectional genetic labeling reveals increased CSN_{TL} axon collateralization in *Lumican* null cervical cord in 5-week-old mice, but not at P15

(A) Schematic illustrating the experimental outline.

(B and C) Immunocytochemistry on axial sections of C3–C4 cervical cord at 5 weeks of age display tdTomato^{+} corticospinal axons labeled by tamoxifen injection at P3 into *Lumican* wild-type or null *Crim1*$^{GCE/+}$;*Emx1*$^{IRES\text{-}Flpo/IRES\text{-}Flpo}$;*Ai65*$^{RCFL\text{-}tdT/RCFL\text{-}tdT}$ mice. Dashed lines demarcate gray matter. Scale bar, 500 μm.

(D) Quantification of relative corticospinal axon collateral density normalized to CST axon number at C1–C2 shows increased CSN_{TL} axon collaterals in *Lumican* null mice compared with wild-type mice throughout the cervical cord. Mean ± SEM, n = 7, Student's t test.

(E and F) Distribution of CSN_{TL} axon collaterals was quantified along mediolateral (E) and dorsoventral (F) axes in wild-type and *Lumican* null cervical gray matter at the C3–C4 level. A representative image is shown to delineate cervical gray matter (dashed line). Mean ± SEM, n = 7, Student's t test. Statistical analysis was performed in each of four bins along each axis. Scale bar, 200 μm.

(G) Immunocytochemistry on axial sections of T1–T2 thoracic cord and L1–L2 lumbar cord collected at 5 weeks of age shows tdTomato^{+} corticospinal axons labeled by tamoxifen injection at P3. Dashed lines demarcate gray matter. Scale bar, 500 μm.

(H) Quantification of CSN_{TL} axon numbers in the dorsal funiculus white matter shows indistinguishable rostral-to-caudal reduction in wild-type and *Lumican* null mice. Mean ± SEM, n = 4, Student's t test.

(I) Quantification of relative CSN_{TL} axon collateral density at T1–T2 and L1–L2 normalized to CST axon number at each respective segment shows indistinguishable CSN_{TL} axon collateral density in *Lumican* null mice compared with wild-type mice. To enable direct comparison, the data for C1–C2 from (D) are reproduced here at this scale. Mean ± SEM, n = 7, Student's t test.

(J) Immunocytochemistry on axial sections of C1–C2 cervical cord at P15 displays tdTomato^{+} corticospinal axons labeled by tamoxifen injection at P3 into wild-type or *Lumican* null $Crim1^{GCE/+}$;$Emx1^{IRES\text{-}Flpo/IRES\text{-}Flpo}$;$Ai65^{RCFL\text{-}tdT/RCFL\text{-}tdT}$ mice. Dashed lines demarcate gray matter. Scale bar, 200 μm.

(K) Quantification of relative corticospinal axon collateral density normalized to CST axon number at C1–C2 shows indistinguishable CSN_{TL} axon collaterals in P15 *Lumican* null mice compared with wild-type mice at C1–C2 and C3–C4. Mean ± SEM, n = 6 (wild type) or 5 (*Lumican* null), Student's t test.

See also Figure S6.

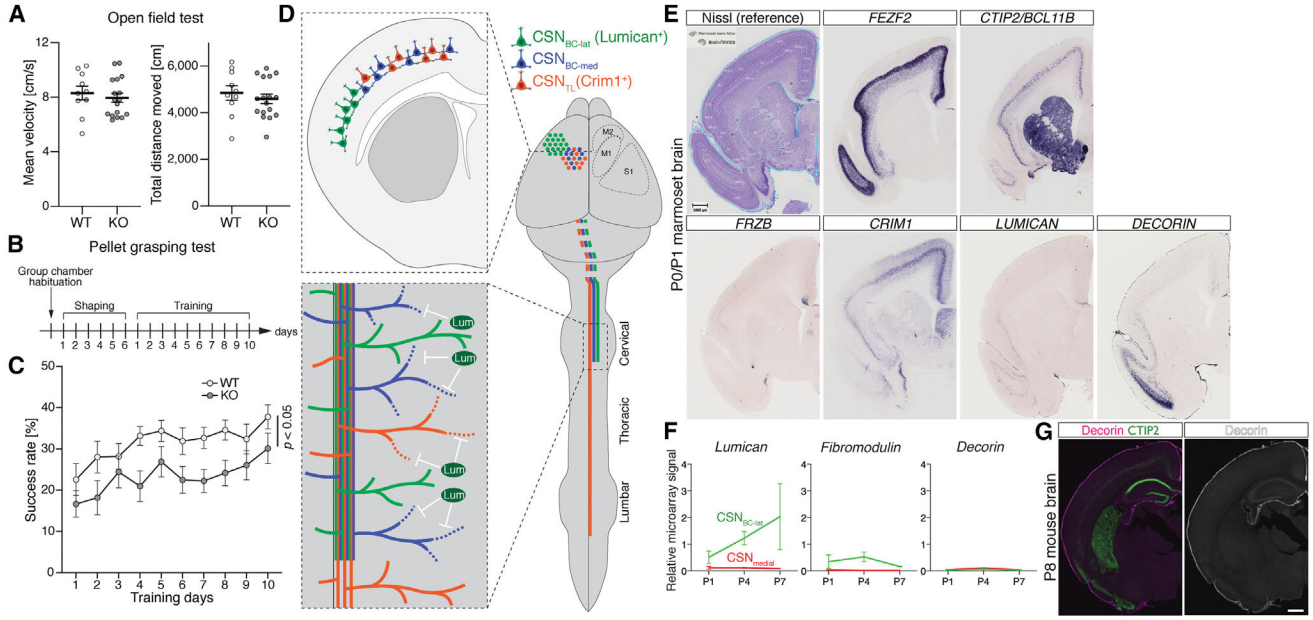

Figure 7. Reduced forelimb dexterity in *Lumican* null mice and expression of SLRP family genes in marmoset and mouse brains suggest expanded use of SLRP genes in mammalian CSN evolution for potentially enhanced forelimb dexterity

(A) Quantification of mean velocity and total distance moved in open field test shows normal gross locomotor activity of *Lumican* null mice. Mean ± SEM, n = 10 (wild type) or 17 (*Lumican* null), Student's t test.

(B and C) A timeline of the pellet grasping test (B). Success rates of pellet grasping during training period show significantly reduced success rate in *Lumican* null mice compared with wild-type mice (C). Mean ± SEM, n = 16 (wild type) or 14 (*Lumican* null), two-way repeated measures ANOVA.

(D) Schematic illustrating inter-axonal molecular crosstalk between molecularly distinct CSN subpopulations. Lumican is expressed by evolutionarily newer $CSN_{BC\text{-}lat}$ (upper inset; green), non-cell-autonomously sculpting axon collateralization by evolutionarily older $CSN_{BC\text{-}med}$ (blue) and CSN_{TL} (orange) in cervical spinal cord (lower inset). $CSN_{BC\text{-}med}$ and CSN_{TL} are interdigitated in medial cortex; axons of all three subpopulations are interdigitated in the CST. Primary (M1) and secondary (M2) motor, and primary somatosensory (S1), cortices are outlined in the right cortex (outlines adapted from Kaas[19]).

(E) Nissl staining and *in situ* hybridization for CSN/SCPN control genes *FEZF2* and *CTIP2*/*BCL11B*, CSN subpopulation-specific genes (*FRZB* for $CSN_{BC\text{-}lat}$ and *CRIM1* for CSN_{medial}/CSN_{TL}, see Sahni et al.[22]), and SLRP family genes *LUMICAN* and *DECORIN* on P0/P1 marmoset coronal brain sections. All images shown here are taken from the Marmoset Gene Atlas website (https://gene-atlas.bminds.brain.riken.jp; experiments AI-1, 78–2, 140–4, 251–7, 262–5, 301–8).[63] Scale bar, 1 mm.

(F) Temporal profile of SLRP family gene expression from microarray analysis.[22] $CSN_{BC\text{-}lat}$, green; CSN_{medial}, red. *Lumican* graph is also shown in Figure 1B. Other than *Lumican*, *Fibromodulin* is the only SLRP gene showing any significant differential expression: *Fibromodulin* expression peaks around P4, although at a much lower level

than *Lumican*. *Decorin* does not show any significant, detectable expression. The y axis represents normalized fluorescence intensity; mean ± SD, n = 2–3.

(G) Immunocytochemistry on coronal section of P8 wild-type mouse brain showing Decorin (magenta) and CTIP2 (green). Apart from meningeal expression, Decorin is not expressed in rostral cortex. Scale bars, 500 μm.

See also Figure S7.

KEY RESOURCES TABLE

REAGENT or RESOURCE	SOURCE	IDENTIFIER
Antibodies		
Goat anti-Lumican	R&D Systems	Cat# AF2745; RRID:AB_2139496
Goat anti-Decorin	R&D Systems	Cat# AF1060; RRID:AB_2090386
Goat anti-Mfge8	R&D Systems	Cat# AF2805; RRID:AB_2281868
Normal Goat IgG Control	R&D Systems	Cat# AB-108-C; RRID:AB_354267
Rabbit anti-Lumican	Abcam	Cat# ab168348; RRID:AB_2920864
Rat anti-CTIP2	Abcam	Cat# ab18465; RRID:AB_2064130
Mouse anti-SATB2	Abcam	Cat# ab51502; RRID:AB_882455
Rabbit anti-TBR1	Abcam	Cat# ab31940; RRID:AB_2200219
Rabbit anti-GFP	Invitrogen	Cat# A11122; RRID:AB_221569
Rabbit anti-RFP	Rockland	Cat# 600–401-379; RRID:AB_2209751
Mouse anti-PECAM-1	Cell Signaling	Cat# 3528S; RRID:AB_2160882
Mouse anti-β-actin	Sigma-Aldrich	Cat# A5441; RRID:AB_476744
Mouse anti-Myc (9E10)	Sigma-Aldrich	Cat# M4439; RRID:AB_439694
Bacterial and virus strains		
AAV-2/1 CAG-EGFP	Vector core at Massachusetts General Hospital, Boston, MA; Maguire et al., 2013[83]	N/A
AAV-2/1 CAG-EGFP-2A-Lumican	This paper	N/A
AAV8 hSyn-EGFP-Cre	UNC Vector core	N/A
AAV Retrograde pmSyn1-EBFP-Cre	Addgene; Madisen et al., 2015[84]	Cat# 51507-AAVrg; RRID:Addgene_51507
AAV1 pCAG-Flex-tdTomato-WPRE	University of Pennsylvania vector core; Addgene; Oh et al., 2014[85]	Cat# 51503; RRID:Addgene_51503
AAV1.hSyn.TurboRFP.WPRE.rBG	University of Pennsylvania vector core (now at Addgene)	N/A
AAV1.CAG.Flex.eGFP.WPRE.bGH	University of Pennsylvania vector core (now at Addgene)	N/A
Chemicals, peptides, and recombinant proteins		
Cholera Toxin B subunit, Alexa 555 conjugate	Thermo Fisher Scientific	C22843
Cholera Toxin B subunit, Alexa 647 conjugate	Thermo Fisher Scientific	C34778
Tamoxifen	Sigma-Aldrich	T5648
10,000 Da lysine-fixable biotinylated dextran-amine	Invitrogen	D1956
3,3′-Diaminobenzidine	Sigma-Aldrich	D4418
Can Get Signal buffer	Toyobo	NKB-201
SuperSignal West Pico PLUS	Thermo Fisher Scientific	34580
FuGene 6	Promega	E2691
Dynabeads Protein G solution	Thermo Fisher Scientific	10003D

REAGENT or RESOURCE	SOURCE	IDENTIFIER
Critical commercial assays		
RNAscope 2.5 HD Assay-RED	ACD Bio	Made to order-Lumican (480361)
ABC-HRP kit	VECTOR laboratories	PK-4000
Amaxa Mouse Neuron Nucleofector kit	Lonza	VPG-1001
Deposited data		
Lumican IP-MS dataset	This paper	Harvard Dataverse repository: https://doi.org/10.7910/DVN/KQQBCN
Mfge8 IP-MS dataset	This paper	Harvard Dataverse repository: https://doi.org/10.7910/DVN/5TCLIO
Experimental models: Cell lines		
HEK293T cells	ATCC	Cat# CRL-3216; RRID:CVCL_0063
Experimental models: Organisms/strains		
Lumican null mouse	Chakravarti et al., 1998[47]	N/A
Fezf2 null mouse	Hirata et al., 2004[86]	N/A
Emx1$^{IRES\text{-}Cre}$ mouse (B6.129S2-*Emx1*$^{tm1(cre)Krj}$/J)	Jackson Laboratory	Stock# 005628; RRID:IMSR_JAX:005628
Crim1^{GCE} mouse	Sahni et al., 2021[22]	N/A
Emx1$^{IRES\text{-}FlpO}$ mouse	Sahni et al., 2021[22]	N/A
Ai65$^{RCFL\text{-}td}$ mouse (B6; 129S-*Gt(ROSA)26Sor*$^{tm65.1(CAG\text{-}tdTomato)Hze}$/j)	Jackson Laboratory	Stock# 021875; RRID:IMSR_JAX:021875
Oligonucleotides		
Lumican in situ probe forward primer; CTCGTTGCTGGTGGTATTACTTC	This paper	N/A
Lumican in situ probe reverse primer; CATGACAGAGGAAAATGACTCAAG	This paper	N/A
Recombinant DNA		
pAAV-EGFP-2A-Stop	This paper	N/A
pAAV-EGFP-2A-Lumican	This paper	N/A
pC3-pro-FLRT3-Fc	O′Sullivan et al., 2012[52]	N/A
pC3-pro-Lumican-Fc	This paper	N/A
pC3-pro-Fc	This paper	N/A
Software and algorithms		
Fiji ImageJ	ImageJ	RRID:SCR_002285
Prism	Graphpad	RRID:SCR_002798
Proteome Discoverer 2.4	Thermo Fisher Scientific	RRID:SCR_014477
DEP	Bioconductor	RRID:SCR_006442
EthoVision XT	Noldus	RRID:SCR_000441